Buckland, H. M., Eychenne, J., Rust, A. C., & Cashman, K. V. (2018). Relating the physical properties of volcanic rocks to the characteristics of ash generated by experimental abrasion. *Journal of Volcanology and Geothermal Research*, *349*, 335-350. https://doi.org/10.1016/j.jvolgeores.2017.11.017

Relating the physical properties of volcanic rocks to the characteristics of ash generated by experimental abrasion

Hannah M. Buckland[a*], Julia Eychenne[b], Alison C. Rust[a] and Katharine V. Cashman[a]

[a] School of Earth Sciences, University of Bristol, Wills Memorial Building, Bristol, BS8 1RJ, UK

[b] Laboratoire Magmas et Volcans, Université Clermont Auvergne - CNRS - IRD, OPGC, Campus Universitaire des Cézeaux, 6 Avenue Blaise Pascal, 63178 Aubière Cedex

***Corresponding author**: hannah.buckland@bristol.ac.uk

Abstract

Interactions between clasts in pyroclastic density currents (PDCs) generate volcanic ash that can be dispersed to the atmosphere in co-PDC plumes, and due to its small size, is far-travelled. We designed a series of experiments to determine the effects of pyroclast vesicularity and crystal content on the efficiency and type of ash generated by abrasion. Two different pyroclastic materials were used: (1) basaltic-andesite pyroclasts from Fuego volcano (Guatemala) with ~26-46% vesicularity and high groundmass crystallinity and (2) tephri-phonolite Avellino pumice (Vesuvius, Italy) with ~55-75% vesicularity and low groundmass crystallinity.

When milled, both clast types produced bimodal grain size distributions with fine ash modes between 4 and 5φ (32-63μm). Although the vesicular Avellino pumice typically generated more ash than the denser Fuego pyroclasts, the ash-generating potential of a single pyroclast was independent of density, and instead governed by heterogeneous crystal and vesicle textures. One consequence of these heterogeneities was to cause the vesicular Avellino clasts to split in addition to abrading, which further enhanced abrasion efficiency. The matrix characteristics also affected ash shape and componentry, which will influence the elutriation and transport properties of ash in the atmosphere. The experimental abrasion successfully replicated some of the characteristics of natural co-PDC ash samples, as shown by similarities in the Adherence Factor, which measures the proportion of attached matrix on phenocrysts, of both the experimentally generated ash and natural co-PDC ash samples. Our results support previous studies, which have shown that abrasion is an effective mechanism for generating fine ash that is similar in size (~5φ; 30μm) to that found in co-PDC deposits. We further show that both the abundance and nature (shape, density, components, size distribution) of those ash particles are strongly controlled by the matrix properties of the abraded pyroclasts.

Keywords

Volcanic ash, abrasion, milling, shape, vesicularity, crystallinity

1. Introduction

Efficient fragmentation of bubbly melt into a dispersion of gas and pyroclasts can generate a large proportion of volcanic ash (Walker, 1981). Most commonly, the process is fuelled by magma overpressure, which generates the explosivity that transforms magma into pyroclasts, often with fractal size distributions (Rust and Cashman, 2011; Turcotte, 1986). Ash can also form, however, by 'secondary fragmentation' (Gonnermann, 2015) within the volcanic conduit (Dufek et al., 2012; Jones et al., 2016), in the thrust region of a volcanic plume (Cioni et al., 2014) or during transport in pyroclastic density currents (PDCs; Dufek and Manga, 2008; Eychenne et al., 2012).

Here we focus on secondary fragmentation in PDCs, where the energetic flow of gas and rock facilitates abrasion and comminution between clasts, as evidenced by the abundance of rounded pumice clasts in PDC deposits (e.g. Manga et al., 2011). These processes generate fine ash, which is important because it affects PDC runout (Dufek and Manga, 2008) and can become buoyant and form a co-PDC plume that disperses the fine fraction into the atmosphere (Engwell et al., 2016; Sparks et al., 1997). These ash particles are hazardous for human health and aviation (Gudmundsson et al., 2012; Horwell, 2007), and can add substantially to the fine ash fraction of the grain size distribution created by primary fragmentation; for this reason, it is important to anticipate the contribution of ash generated in PDCs to the total ash budget produced by an eruption. Previous studies show that the amount of ash generated by abrasion in PDCs will depend on a variety of factors such as the material in the PDC, the flow conditions and background eruptive behaviour (e.g., Gravina et al., 2004; Kueppers et al., 2012; Manga et al., 2011). Here we analyse the effects of pyroclast vesicularity and crystal content on the efficiency and type of ash generated by abrasion. We take an experimental approach, following previous studies that imitate abrasion in PDCs (Kueppers et al., 2012; Manga et al., 2011; Mueller et al., 2015). We extend these studies by using variably crystalline starting material and by quantifying the amount of ash generated, as well as the ash size, componentry and shape, as these parameters influence the particle settling behaviour and therefore both elutriation and transport potential in the atmosphere (Coltelli et al., 2008).

2. Background

Secondary fragmentation in PDCs has the potential to alter the total grain size distribution (TGSD) of an eruption (Rose and Durant, 2009). Specifically, the small mean grain size of co-PDC ash (typically <63 μm; Engwell and Eychenne, 2016; Marti et al., 2016) increases the power law exponent of the grain size distribution (Jones et al., 2016). These small ash particles can travel long distances in the atmosphere (Engwell et al., 2014), such that co-PDC ash is often the furthest travelled ash from large ignimbrite-forming eruptions (Engwell and Eychenne, 2016). Consequently, understanding ash formation by secondary processes, such as abrasion in PDCs, is key for predicting the ash size distribution and ash dispersion potential of future PDC-generating eruptions.

The typically smooth shapes of pumice clasts in PDCs, regardless of distance of transport, indicate that clast rounding and, by inference, peak ash production, is rapid and takes place close to the vent (Manga et al., 2011). Experiments have replicated the rounding of pumice clasts observed in PDC deposits and the change in clast shape during abrasion has been related to the amount of ash generated in the flow (Dufek and Manga, 2008; Manga et al., 2011). Importantly, these experiments found that the maximum extent of clast rounding is not simply a function of the mass removed by abrasion. In fact, peak clast rounding can occur when clasts have lost between 15% and 60% of their initial mass. The broad range in the mass loss indicates that the peak ash production must be related, to some extent, to the properties of the abrading material.

The effect of clast vesicularity on the efficiency of ash generation has also been examined experimentally (Kueppers et al., 2012; Mueller et al., 2015), with low-density (vesicular) clasts generating more ash than denser (less vesicular) clasts when subjected to the same duration of milling in a rock tumbler. Here we suggest, however, that the differences in ash production are controlled not only by differences in vesicularity, but also by the crystal content (size, shape and abundance of phenocrysts and microlites). As PDC components from different volcanoes are extremely varied in both vesicularity and crystal content, both properties must be assessed to anticipate the ash-generating potential of a specific PDC.

Experiments have shown that the shape of ash is also altered by abrasion (Jones et al., 2016). In an experimental study using a ball mill, Jones et al. (2016) found that increased milling duration produced

ash particles with higher axial ratios (more equant shapes), which indicates the progressive rounding of ash grains, as well as increased removal of matrix from phenocrysts and phenocryst fragments (Freundt and Schmincke, 1992; Jones et al., 2016). From this perspective, it is possible that the shape and internal texture of ash generated by abrasion could be used to distinguish it from ash generated by the primary fragmentation of the magma. Field studies of the Latera Volcanic Complex, Italy, have shown that sanidine crystals in the PDC deposit have fewer boundary irregularities than crystals of the same grain size in the fall deposit (Taddeucci and Palladino, 2002). Similarly, a preliminary assessment by Liu et al. (2015a) of Tambora ash suggests that co-PDC ash particles have grain boundaries with reduced roughness compared to fall-deposit ash of the same grain size.

The phenocryst content should also affect the efficiency of ash generation by abrasion, as crystals can influence fracture and breakage patterns in pyroclasts (Wawersik and Fairhurst, 1970). However, the effect of phenocrysts is not clear. Crystals may either resist erosional processes such as abrasion in mass flows, or conversely, may introduce planes of weakness, especially if they have platy textures or have been fractured by the initial brittle fragmentation (Bindeman, 2005; Thomson et al., 2013). For instance, experiments show that crystal-rich pyroclasts from Mount Unzen are more resistant to abrasion than less crystalline samples (Kueppers et al., 2012). Similarly, crystal-bearing Medicine Lake pumice abraded more slowly than crystal-free, texturally homogenous Taupo pumice of similar density (Manga et al., 2011). What still is unclear, however, is the effect of a heterogenous distribution of phenocrysts and microlites, such as localised dense zones within a pumice clast, on the characteristics of ash generated by abrasion.

Also unexplored is the effect of groundmass crystallinity (i.e. microlite content) on the resistance of pyroclasts to abrasion. Hydrous mafic (basalt, basaltic andesite) magmas, in particular, experience extensive groundmass crystallization during rapid magma ascent in the conduit (e.g., Shea and Hammer, 2013). The products of these eruptions also have total grain size distributions (TGSDs) with less fine ash than their microlite-free counterparts (Durant and Rose, 2009; Jones et al., 2016; Rust and Cashman, 2011; Turcotte, 1986), which suggests that microlites affect primary fragmentation. We expect the role of groundmass crystallinity in secondary fragmentation processes to be four-fold. First, microlite-rich

120 samples also have low vesicularities, which would suggest that they should resist abrasion. Second,
121 these samples have thick bubble walls, so that even if they abrade, the ash particles should be larger
122 than in low crystallinity, high vesicularity samples. Third, analogue and numerical experiments
123 (Oppenheimer et al., 2015; Parmigiani et al., 2016, 2011) show that groundmass crystals aid formation
124 of gas pathways, which could control patterns of breakage. Finally, the crystal content of the resultant
125 ash influences ash shape, as crystalline ash is typically blocky and lacks the perimeter concavities
126 caused by abundant vesicles (Liu et al., 2015).

127 In this study, we test the efficiency of secondary ash generation by abrasion as a function of both
128 vesicularity and crystallinity (phenocrysts and groundmass) of starting pyroclasts. We use samples
129 from a violent Strombolian eruption of basaltic andesite Volcan Fuego, Guatemala, and from the Plinian
130 Avellino eruption of tephra-phonolite from Vesuvius volcano, Italy. Informed by previous studies
131 (Kueppers et al., 2012; Manga et al., 2011) we expected that the low density (high vesicularity) Avellino
132 pumice would generate more ash than the high density (low vesicularity) Fuego pyroclasts. To test this
133 hypothesis, we characterised the size, shape, vesicularity and crystallinity of the products both prior to
134 and following abrasion experiments to dissect the links between the crystallinity, ash generation and
135 ash shape. We then compare experimental and natural ash particles to assess the reliability of ash shape
136 as an indicator of fragmentation process.

137 ### 2.1 Volcan de Fuego (2012 eruption)

138 Volcan de Fuego is a stratovolcano located along the Central American volcanic arc in Guatemala. It
139 produces frequent discrete violent Strombolian blasts with small ash plumes (<10km) and lava flows.
140 Occasional 'paroxysms' of heightened activity generate Vulcanian to sub Plinian eruption columns and
141 PDCs (Rose et al., 2008). The material used in our experiments is from a paroxysmal eruption in
142 September 2012, which was more explosive than typical Strombolian activity (Chigna et al., 2012).
143 The eruption produced a block and ash flow that we sampled ~6km from the vent on a field campaign
144 in March 2016. The deposit is massive, poorly sorted and contains large blocks of basaltic andesite.
145 We assume that the material is geochemically similar to basaltic-andesite explosive products from the

1974 eruption of Fuego (Chesner and Rose, 1984) as no geochemical analyses have been carried out on the 2012 eruptive products. This assumption is supported by the similarity of the phase assemblage to the 1974 material, and the lack of compositional differences between magma erupted in 1974, 1999 and 2003 (Berlo et al., 2012). Major element analyses of the 1974 pyroclasts show an average silica content of 56.5 wt% and a total alkali content ($Na_2O + K_2O$) of ~5.6 wt% (Chesner and Rose, 1984).

Additional material from Volcan de Fuego used in this study includes 2012 ash that was sampled from the top of a small block and ash flow. The ash represents the dilute portion of the PDC that settled out after the emplacement of the dense basal layer and is termed "PDC-surge" ash henceforth. The 3φ (177-125μm) fraction of this PDC-surge ash was imaged by E. Liu (*personal comm*). As a reference, we also analyse fall deposit ash generated during a paroxysm of Fuego in 2016 (sampled by E. Liu).

2.2 Pomici de Avellino (3.9ka B.P.)

An eruption of Somma-Vesuvius, Italy in 3.9ka B.P produced the Pomici de Avellino (PdA) deposit (Sulpizio et al., 2008). It was a large explosive eruption characterised by three distinct eruptive phases: an opening Plinian phase followed by a column collapse phase and a final phreatomagmatic phase (Sulpizio et al., 2010a). The stratigraphy is split into eruption units EU1 to 5 (Cioni et al., 1999). The products used in our experiments are from a PDC from EU3 that was generated during the column collapse phase. The PDC from this phase (EU3pf) was directed to the north, had a short runout (<10km) compared to the later EU5 PDCs (>20km, Sulpizio et al., 2010b) and is described as 'poorly sorted massive to stratified lapilli and ash' (Sulpizio et al., 2010b). Analyses of Avellino EU3 glasses by Sulpizio et al. (2010b) yield an average silica content of 55.6 wt% and a total alkali content of 12.8 wt%, classifying the products as tephri-phonolite.

No distinct co-PDC or surge ash layer is found in the Avellino EU3 deposit (Sulpizio et al., 2010a). Instead, ash from the matrix of the dense part of the EU3pf deposit was sampled to compare to our experimentally generated ash and to examine the results of natural abrasion during transport in the flow.

3. Methods

3.1. Characterisation of starting materials

3.1.1. Density

Juvenile clast densities were measured using the methodology of Houghton and Wilson (1989). Removable paraffin film of known density was used to seal the clasts for the density measurements which enabled clasts of known density to be later used in the abrasion experiments. The density distributions of the Fuego and Avellino clasts in the -3φ (8-16mm) size range that we used as starting material are shown in Figure 1. The mean densities of the Fuego and Avellino pyroclasts are 1.92 gcm^{-3} and 0.97 gcm^{-3}, respectively. Each sample was divided into three sub-samples for the abrasion experiments (Fig. 1): one with a density close to the average of the bulk juveniles (AD), one with lower than mean density (LD) and the third with a higher than mean density (HD). This was done to test whether LD clasts (high vesicularity) generate more ash than the HD (low vesicularity) clasts. To track the change in shape of the large clasts (e.g., Manga et al., 2011), the clasts in each sub-sample were placed on a light board in order of ascending density and photographed before and after each abrasion experiment.

Dense rock equivalent (DRE) densities are required for calculating vesicularity. The Avellino DRE density used was 2.42 gcm^{-3} (Balcone-Boissard et al., 2012). The DRE density for Fuego was approximated from a dense juvenile, measured at 2.79 gcm^{-3} (Houghton and Wilson, 1989).

3.1.2. Vesicularity

The vesicularity 'V_D' was calculated using the DRE densities of Avellino and Fuego lavas and the measured juvenile densities (e.g., Houghton and Wilson, 1989; Fig. 1). The average V_D calculated for Fuego was 31.2% and 59.6% for Avellino.

We also measured the vesicularity from polished thin sections of juvenile clasts (-3φ), as imaged using a Hitachi S-3500N Scanning Electron Microscope (SEM) at the University of Bristol in backscattered

electron (BSE) mode. Imaging the clasts at several magnifications ensured the optimum resolution for subsequent image analysis of both vesicles and crystals (Shea et al., 2010). Vesicularity and bubble number density (BND) were calculated from BSE images using FOAMS, a MATLAB™ based program (Shea et al., 2010) that converts 2D BSE images into a 3D representation of the vesicularity, 'V_F'. The average vesicularity of four Fuego juvenile clasts was 32.4%, which is similar to the average measured V_D. It was not possible to determine an accurate V_F for the EU3pf pumice using FOAMs because of the heterogeneity of the vesicle population. The measured V_F of pumice from the EU3 fall deposit is 56.1% (Voarino, 2016), which is similar to the V_D value of 59.6%. This, together with the close agreement of V_D and V_F for Fuego, gives us confidence in the robustness of the density measurements.

3.1.3. Crystal Content

The phenocryst content of the starting materials was quantified using the BSE images acquired for vesicularity. Additional high magnification (1500x) BSE images were used to quantify the microlite content of the samples. Crystal identities were checked by energy dispersive spectroscopy (EDS) spot analyses on the SEM, after which the BSE grey scale value of each phase was used to map the phase distribution. The abundance of each phenocryst phase and the ratio of microlites to glass in the groundmass on a vesicle-free basis were determined with ImageJ.

3.2 Abrasion Experiments

The abrasion experiments were carried out using a planetary ball mill manufactured by Retsch Ltd. The Retsch Ltd PM 100 model has a vertical axis of rotation. This differs from studies in which a rock tumbler was used (Kueppers et al., 2012; Manga et al., 2011), where the rotation axis was horizontal. Typically, the Retsch planetary ball mill is used to generate very fine powders due to the milling efficiency that results from high centrifugal forces generated at high milling speeds (Mio et al., 2002). We did not want complete pulverisation of the samples, therefore short milling times were used (4-5 mins). Additionally, the agate milling balls that encourage high energy impacts across the milling jar (Lu et al., 2012) were excluded, which means that the milling produces only clast-to-clast and clast-to-jar-wall interactions. We assume that friction at the jar walls is minimal due to the small mass of a

single clast and the smooth nature of the agate lined jar (Kueppers et al., 2012) and that the abrasion is driven mainly by clast interactions (both frictional sliding and impacts).

Sub-samples with an initial grain size of -3φ (8-16mm) were used in the abrasion experiments. This ensured that all post-milling material smaller than the starting grain size was generated in the experiment. The number of clasts in each experiment was limited by the size of the grinding jar and the availability of material in the -3φ fraction (Table 1). The grinding jar was sealed, placed on the rotating base and milled for 4 minutes with a rotation rate of 450 rpm (Fig. 2). Two additional Avellino abrasion experiments were carried out to investigate the effect of varying the starting grain size and the addition of a lithic component (sample Av31b and Av3AG, respectively; Table 1).

Our aim is to simulate processes occurring as clasts are transported in a PDC. The equivalent transport distance (x) of the milling,

$$x = l \cdot t \cdot v, \qquad (1)$$

is ~425m for our experiments, with l being the inner milling jar circumference, t is the milling time in mins and v is the rotation rate in rpm (Kueppers et al., 2012). The speed at the wall of the rotating jar ($= x / t$) was ~6.5km/hr which is an order of magnitude lower than typical PDC ground velocities (e.g., Cole et al., 2002). However, the velocities of the clasts relative to each other during milling, are much higher due to the planetary ball mill configuration (>20km/h, Lu et al., 2012) and more comparable to the internal velocities in a natural PDC.

3.3 Characterisation of experimental products

3.3.1. Grain size distributions (GSDs)

The milled samples were manually dry-sieved from -3 to 3 phi (φ), with half phi sieving performed where possible. The size distribution of the fine material (>2φ, <250μm) was quantified using a Mastersizer 3000™ by Malvern Instruments Ltd in the School of Geographical Sciences at the

University of Bristol. The fine and coarse fractions were combined to produce a GSD for each experiment using the overlap in the 3φ size fraction (e.g., Jones et al., 2016).

3.3.2. Sample preparation and analysis conditions

After milling, grains from each size fraction were mounted and polished separately to ensure that all ash particles could be imaged at the same magnification (Liu et al., 2015a). When imaging the ash mounts, the objective was to balance the resolution of the images and the number of grains imaged. Typically, we found that at a working distance of ~ 15mm, an accelerating voltage of 15 or 20kV and 200x magnification gave an optimum resolution (~ 1560 pixels/mm). Automated grid images, typically made up of 20-60 individual images, were stitched together using the ImageJ stitching plugin. The collated images contain 400-1000 grains with 30,000-60,000 pixels per grain. The ash componentry was then assessed from the BSE grid images with grains classified as free crystals, crystals with attached melt or matrix, groundmass grains, vesicular glass or pure glass.

3.3.3. Post-abrasion analysis of large clasts

The largest clasts (-3 and -2φ) remaining after the abrasion experiments were photographed and their size and shape compared with the original clasts of the same sub-sample. It was not possible to match each individual clast pre- and post-abrasion, therefore we amassed the shape data for all the sub-samples of each starting material and compared the average change in shape. We used the metric form factor 'FF' (Liu et al., 2015; termed 'R' in Manga et al., 2011) to measure shape, where FF = 1 represents a perfect circle (Table 2):

$$FF = 4\pi * \text{area of particle} / (\text{perimeter of particle})^2. \quad (2)$$

The results of the shape analysis, particularly whether the FF increased (rounded) or decreased, informed our choice of which remaining clasts to mount for vesicularity and crystallinity characterization. As both starting materials were sampled from PDC deposits, the clasts had already experienced some degree of natural abrasion. The change in FF of the larger clasts from pre- to post-abrasion could therefore represent the effect of further transport in a natural flow.

3.3.4. Ash shape analysis

The BSE grid images gathered for componentry analysis were also used to measure particle shape. Images were first cleaned and converted to a binary form, then ash shape was measured using an ImageJ macro from Liu et al. (2015a). The natural ash samples from Fuego and Avellino (Table 1) were sieved, the 3φ fraction imaged, and the cross-sectional shape measured using the same approach used for the experimentally generated ash. For comparison purposes, the resolution of the BSE images of the experimental ash was reduced to match the Fuego PDC-surge ash images (~390 pixels/mm, E. Liu, *personal comm*.), as convexity is sensitive to perimeter resolution. This was done by reducing the image size in ImageJ, which resamples the original image using bilinear interpolation (Ferreira and Rasband, 2012). The image analysis and shape measurements were then repeated using the lower resolution images. Table 2 outlines the key shape parameters used in this study. Grains classified as 'crystals with attached matrix' in the componentry analysis were further analysed to determine the 'Adherence Factor' (AF; Jones et al., 2016):

$$AF = (\text{area of matrix}) / (\text{area of matrix} + \text{area of crystal}). \quad (3)$$

Values of AF close to 1 reflect a large proportion of attached matrix. This measurement required further manipulation of the BSE grid images to enhance the grey scale contrast between attached matrix and crystal.

The projected area of the experimental ash particles was measured using Morphologi G3SE™ by Malvern Instruments Ltd, an Optical Particle Analyser (OPA) located in the Laboratoire Magmas et Volcans, Clermont-Ferrand, France. Morphologi homogeneously disperses dry particles onto a glass plate using compressed air. The ash is then imaged and basic size and shape parameters of individual grains are measured using the same metrics in Table 2 (Leibrandt and Le Pennec, 2015). We analysed the 3φ fraction of Fuego sample F3a and Avellino sample Av31a (Table 1) to compare with the results of the 2D shape analysis. The 4φ (74-63 μm) fraction of these samples was also analysed to compare the shape measurements made across the two grain size fractions. The 4φ fractions were sieved by

quarter phi increments, cleaned with ethanol and dried prior to analysis to ensure that very fine material was removed.

For each starting material and grain size, a standard operating procedure (SOP) was designed. The light source (diascopic or episcopic), magnification, focus, threshold and the area of the dispersion to scan were set manually (Leibrandt and Le Pennec, 2015). We concluded that the best resolution was provided by using a 5x optic with diascopic light (light from below) to obtain the 2D projected area of the ash shape. Once the SOP was defined, each analysis took 30-40 minutes depending on the scanning area.

Following the automated analysis, the Morphologi software (Malvern) generates an output file of the shape and grain size data. The 3φ size fraction produced grain counts of 3000-7000, and the 4φ analyses contained over 10 000 grains per sample. The output files required cleaning due to the imperfect nature of the imaging and automated dispersion (see Fig. S1). Grain counts in the 4φ fraction were reduced to a sub-sample of 6000 randomly selected grains before the anomalous grains were removed. This ensured the same degree of manual error in the datasets of each grain size fraction.

4. Results

4.1. Sample characterisation

On a vesicle-free basis, Fuego pyroclasts have ~35% phenocrysts, but the phenocryst content ranges from 41% in a HD clast to 30% in a LD clast. The phenocrysts are dominantly plagioclase and olivine with sizes of 0.3-4mm. The average microlite content is ~40% in the groundmass (on vesicle-free basis) and comprises plagioclase (dominant), clinopyroxene, oxides and olivine. There is minor variability, but no significant difference in the microlite crystallinity between the high- and low-density sub-samples.

The vesicle size distribution (VSD) varies with density in the Fuego pyroclastic starting material. We prepared and imaged LD, AD (average density) and HD Fuego pyroclasts (Fig. 3) to analyse with FOAMS (Shea et al., 2010). There is a general trend of larger vesicle sizes and thicker bubble walls

with increasing density. The modal vesicle size of the HD clasts (Table 1) is 1-0φ (0.5-1mm), with no vesicles <5φ (0.031mm) (Fig. 3d, h). LD clasts have a substantial fraction of bubbles (by area and by number) <2φmm (0.25mm) and a modal vesicle size between 3-2φ (Fig. 3a,b). Some LD clasts have a small number of large vesicles (>0φ) which account for a large area fraction (Fig. 3b, f). These clasts with large vesicles (Fig. 3b) also have more glomerocrysts and higher groundmass crystallinity than other LD clasts (Fig. 3a). From examining a small number of LD clasts (6), it appears the two types of LD textures (Fig. 3e, f) occur in equal proportion in the Fuego pyroclasts.

The average (vesicle-free) phenocryst crystallinity of the Avellino pyroclasts is ~12%, ranging from 8% in an LD pumice clast to a maximum of 20% in an HD pumice clast. The phenocrysts in the Avellino pumices are 0.2-1.5mm in size and dominantly sanidine and nepheline with minor amphibole, vesuvianite and clinopyroxene. The microlite content on a phenocryst and vesicle-free basis is 7-13%, and comprises sanidine, nepheline and minor skeletal leucites (Voarino, 2016). Spatial variations in microlite content include microlite-rich areas that are most frequent in the HD clasts (Fig. 4a and b). There are also fragments of thermally recrystallised limestone embedded in the pumice associated with large vesicles, which likely result from volatile release due to thermal decomposition of carbonate minerals (Fig. 4c, e.g. Jolis et al., 2015; Sottili et al., 2010). Leucite microlites and the dense microlite-rich areas appear to be unique to the dense mode of the EU3pf deposit (Voarino, 2016).

4.2. Grain size distributions

All post-abrasion grain size distributions (GSDs) are bimodal, with most of the resultant ash ≤ 125μm (≥3φ; Fig. 5). Details of the GSDs differ, however, in that the fine mode lies at 4φ (63-90μm) in the Fuego experiments and 5φ (32-45μm) in the Avellino experiments. Moreover, the Avellino clasts generally produce more ash than the Fuego clasts. Cumulative grainsize distributions for all experiments are shown in Figure 6, where the y-axis represents the starting grain size (-3φ). These distribution profiles highlight another consistent difference between Fuego and Avellino samples. The relatively flat profiles of the Fuego GSDs across the intermediate grain size fractions (-1 to 3φ) shows negligible formation of ash of intermediate size. In contrast, the Avellino GSDs do not have flat profiles between -1 and 3φ, meaning that milling generated particles across a wide range of grain sizes.

346 Overall, the Fuego milling experiments generated less ash than the Avellino experiments. In detail
347 however, the response of individual Fuego pyroclasts to abrasion varies. The expected result was that
348 the high density (low V_D) sub-samples would generate the least ash and the low density (high V_D) the
349 most. For example, experiment F3a behaved as expected: >60% of the material generated in the LD
350 experiment was smaller than -3φ, whereas <16% of the material in the HD experiment was smaller than
351 -3φ. However, most experiments did not show this behaviour: there are other Fuego experiments where
352 LD sub-samples (highest V_D), do not generate the highest proportion of ash (e.g., F2a; Fig. 5c).
353 Similarly, the HD sub-samples, which contain clasts with high crystal contents (both phenocrysts and
354 microlites) and low V_D, are not always the most resistant to abrasion.

355 Crystal-poor, high vesicularity Avellino experiments consistently have a smaller proportion of the
356 material remaining in the -3φ fraction than the experiments with crystal-rich, vesicle poor Fuego
357 material. This indicates more efficient abrasion and ash generation for pyroclasts with low crystallinity
358 and high vesicularity. We still see variability in the amount of ash generated, however. In one extreme,
359 LD sub-sample Av31a yields <10% of mass remaining in the starting grain size, while milling of the
360 AD (average density) sub-sample generated less ash (>40% of the material remaining in the starting
361 size) than the HD sub-sample (Fig. 5d).

362 **4.3. Abrasion products**

363 4.3.1. Shapes of large clasts

364 The median form factor (FF) of all large (-3 and -2φ) clasts increased after milling (Fig. 7), reflecting
365 the expected clast rounding due to abrasion (Manga et al., 2011). Although the median FF values
366 increase, post-abrasion clast shapes are variable. At the same time, some experiments show an increase
367 in the number of grains in the -3 and -2φ grainsize fractions (see Table 1; Fig. 7). For example, milling
368 of Av33a HD caused the number of large clasts to increase from 7 to 9. Both the range in FF values and
369 the increase in particle number can be explained by splitting, rather than solely abrasion, of clasts.
370 Splitting of clasts also explains the low (outlier) FF measurements in the Avellino data (Fig. 7) that
371 indicate an increase in clast angularity.

372 4.3.2. Projected area ash analysis from Morphologi

373 Ash shape measurements of the 3φ AD sub-samples are shown in convexity (CVX) - solidity (SLD)-
374 plots in Figure 8a, b (see Fig. S2 for 4φ shape data). The shape data based on Morphologi images are
375 concentrated at high-CVX and high-SLD values, as illustrated by the 20% contour of Fuego data, which
376 plots between SLD values of 0.94-0.98 and CVX values of 0.95-0.98 for all the sub-samples. The same
377 contour of the Avellino shape data plots between SLD and CVX values of ~0.95-0.98. In the extreme,
378 however, the Avellino contour plots show a somewhat greater range, particularly in convexity. For
379 example, the Avellino 90% contour extends to convexities of ~ 0.87, whereas the Fuego 90% contour
380 does not reach below CVX = 0.90.

381 Ash componentry was also evaluated using the Morphologi images, with categories designated as free
382 crystal, vesicular, opaque (likely matrix dominated), crystal with attached melt or, in some cases,
383 'unknown'. The categorisation was done on a random selection of 500 grains per sample. The
384 convexity and solidity values of these 500 grains are plotted in Figure 8c, d. The Fuego ash comprises
385 mostly free crystals and opaque grains. The free crystals (red diamonds) typically record the highest
386 SLD and CVX; opaque grains have a broader range in SLD and CVX. In the Avellino samples,
387 vesicular grains (green asterisks) are numerous and plot with lower SLD and CVX values than the rest
388 of the grains, reflecting the irregular outlines of these particles.

389 4.3.3. Cross-sectional area (BSE) ash analysis

390 BSE images of polished 2D sections provide a more nuanced measure of particle shape as well as details
391 of the internal textures of individual grains (Liu et al., 2015a). Again, we plot CVX vs. SLD of 3φ grains
392 from post-milling samples F3a and Av31a (Fig. 9). As anticipated, SLD and CVX measured on 2D
393 images of cross-sections are much lower and more varied than the projected area (Morphologi) results.
394 Note the more limited number of grains analysed (lower n values) compared to Figure 8 are because
395 sample preparation and BSE image acquisition are more time consuming than Morphologi analyses.
396 The Fuego ash ranges from 0.39-0.96 SLD and 0.50-0.95 CVX. The Avellino ash covers an even wider
397 spectrum, with SLD ranging from 0.22 to 0.97 and CVX from 0.21-0.97.

Componentry analysis of the same particles (Fig. 10, Fig. S3) helps to explain the shape parameter range. Fuego ash is dominated by variably crystalline matrix fragments, with >50% of the grains being groundmass grains that have CVX and SLD values of ~0.75 – 0.9. Conversely, Avellino ash comprises predominantly free crystals and vesicular grains, the former having very high CVX and SLD values, and the latter marking the low CVX and SLD extremes.

The differences between the shape parameters measured by ImageJ and Morphologi reflect the differences between cross-sectional area and projected area (Liu et al., 2015a). Lower and more varied values of convexity and solidity are measured using BSE images and ImageJ due to the ability to measure small-scale roughness. The most extreme ash shapes measured by both methods (lowest values of CVX and SLD) are the vesicular grains that characterize the microlite-poor Avellino samples. The free crystals, in contrast, yield the highest SLD and CVX values (>0.95 in Fig. 8 and >0.8 in Fig. 9) using both methods, and thus provide an approximate measure of the free crystal content of individual ash samples.

4.3.4 Natural ash samples

Two natural Fuego ash samples were analysed for their shape (Fig. 11a, b). The Fuego 2016 fall ash contains more grains with lower SLD and CVX values than the experimental or natural PDC-surge ash (Fig. 11). Similar to the experimental Fuego ash, the natural fall and surge ash show a range in microlite textures with an average microlite content of ~41%, comparable to the crystallinity measured from Fuego pyroclasts used in the experiments.

The CVX-SLD density plot of the natural PDC-surge and experimental Avellino ash (Fig. 11c) shows a slight increase in the number of low SLD and CVX values in the experimental ash compared to the natural ash. An important difference between the two samples is the presence of holocrystalline ash grains in the natural ash, which comprise ~29% of the components (Fig. 11f). They are the remnants of lithics that were incorporated into the Avellino PDC.

4.3.5 Adherence Factor

Experimental ash from both Fuego and Avellino contained numerous ash grains that were classified as 'crystals with attached matrix' (Fig. 10). We quantified the amount of matrix attached to each imaged crystal in the 3φ size class using the 'Adherence Factor' (AF; Eq. 3). As shown in Figure 12, the Avellino and Fuego samples show contrasting AF distributions. Avellino ash samples yield the lowest AF values, whereas the Fuego samples, show a wide range of AF values. For comparison, we also include the results of milling experiments on Soufriere Hills Volcano (SHV) pumice (Jones et al., 2016) which has intermediate values of vesicularity and crystallinity, and correspondingly intermediate AF trends.

5. Discussion

The abrasion experiments show that, for the same duration of milling, the Avellino pumice generated more ash than the denser Fuego juvenile material (Figs. 5 and 6). This supports the results of Kueppers et al. (2012), who found that material of lower density and higher vesicularity generates more ash when abraded. However, the results are less straightforward when the starting material is examined in the context of density-designated sub-samples from the same eruption. This means that density alone cannot be used to predict the behaviour of material subjected to abrasion. Moreover, our experiments show that ash shape, size and componentry vary both within and between samples. As these parameters determine the transport properties of secondary ash particles, understanding controls on these properties is critical for predicting the contributions of co-PDC ash to distal ash clouds.

5.1 Effects of pyroclast textural heterogeneity on abrasion

5.1.1 Fuego pyroclasts

The vesicle size distribution (VSD) of pyroclasts influences the TGSD generated by primary fragmentation (Liu et al., 2015b; Rust and Cashman, 2011). The VSD of pyroclasts may also affect the extent of secondary fragmentation because vesicles affect brittle rock strength (Heap et al., 2014) and form zones of weakness that may control patterns of breakage. Sub-samples in the Fuego experiments, in particular, display a wide range in the amount of ash generated, which likely reflects VSD variations in the Fuego starting material (Fig. 3). If clasts abrade by fracturing at the weakest point, which

449 typically will be the thinnest part of a vesicle wall, then the low vesicle number density and increased
450 thickness of the bubble walls in the HD samples explains the resistance to abrasion of the HD clasts.
451 The average bubble wall thickness may also control the size of the abraded ash particles (typically 4φ,
452 or ~63 μm, in Fuego LD samples).

453 Not all Fuego LD clasts generated a large proportion of ash when abraded (Fig. 5c), however. To
454 address this discrepancy, we imaged two post-milling LD clasts of similar density: one that recorded a
455 25% decrease in projected area with visible rounding (Fig. 3a) and one that recorded only a 2% decrease
456 in projected area and showed a decrease in FF post-milling, rather than the expected increase (Fig. 3b).
457 The clast that did not round (Fig. 3b) has a smaller modal vesicle size, elevated microlite crystallinity
458 and a greater number of phenocrysts, glomerocrysts and large vesicles compared to the LD clast that
459 did round (Fig. 3a). Here the few large vesicles (~0.5mm; Fig. 3b) allow the non-rounded clast to retain
460 a low density, whilst the high crystallinity (both glomerocrysts and microlites) controls its resistance to
461 abrasion. It seems likely that the relative proportions of these two clast types in the LD sub-samples
462 explains the range in ash production rates. The importance of heterogeneities in ash generation means
463 that our individual experiments with a small number of clasts are not representative; however, the
464 limited set of clasts allows us to explore the differences in sub-samples by isolating individual clasts,
465 monitoring their behaviour post-milling and attributing differences in behaviour to differences in
466 vesicularity and crystal content.

467 5.1.2 Avellino pyroclasts

468 The Avellino experiments consistently generated a higher proportion of ash than the experiments with
469 denser Fuego pyroclasts. Interestingly, however, the HD sub-samples generated more ash than the AD
470 sub-samples in two of the Avellino experiments, contrary to the expectation that high density (low
471 vesicularity) clasts would be most resistant to abrasion (Kueppers et al., 2012). Sectioning of selected
472 clasts shows that the EU3pf pumice is highly heterogeneous in both vesicularity and crystal content,
473 particularly in the HD clasts. For example, HD clasts can contain microlite-rich zones that have a high
474 number density of microlites and low vesicularity relative to the surrounding melt (Fig. 4a, b; Voarino,

2016), textural features that should make these zones relatively resistant to abrasion, leading us to further question the high proportion of ash generated by two of the HD sub-samples.

The -2φ fraction of the EU3pf deposit has a bimodal density distribution, unlike the -3φ fraction, with a secondary dense mode created by clasts with relatively high microlite content (Voarino, 2016). To test the response to abrasion of microlite-rich clasts, we carried out an additional abrasion experiment using the dense Avellino pumices from the -2φ fraction (sample Av31b in Table 1). The resulting GSD (Fig. 6c) shows that the clasts were less abraded than the -3φ clasts even when milled for an extra minute, confirming that the increased microlite content of the -2φ strongly enhances their resistance to abrasion. However, the extremely microlite-rich zones (Fig. 4), were only present in two out of five HD clasts imaged post-abrasion. Therefore, rather than limiting abrasion, the HD clasts which have elevated microlite content or contain dense zones could increase abrasion by acting as resistant grains that abrade the more vesicular clasts. This is analogous to the scenario where a lithic component (i.e. more resistant lithology) incorporated in PDCs encourages efficient abrasion (Bernard and Le Pennec, 2016). This may be one explanation for the unexpected behaviour of some HD subsamples (Fig. 5,6).

Additional heterogeneities in Avellino clasts include xenoliths of altered limestone, which generate cavities in the surrounding melt by decarbonation (Fig. 4c). These cavities introduce internal weaknesses that may promote clast splitting rather than abrasion (see section 5.2).

The heterogeneities observed within the Fuego and Avellino pyroclasts are typical of the textural heterogeneity found in natural PDC material (e.g. Bernard and Le Pennec, 2016; Gardner et al., 1998). Importantly we have shown that textural heterogeneity within a density class from a single eruption can influence pyroclast resistance to abrasion. The demonstrated sensitivity of clast abrasion to internal heterogeneities means that density alone cannot be used to predict the efficiency of ash production by abrasion within a PDC.

5.2 Enhanced ash production due to clast splitting

The increase in the post-milling clast count in the -2φ and -3φ fractions (Table 1) indicates that some clasts split during the abrasion experiments. Clast splitting can facilitate further abrasion, as it increases

501 the total surface area and number of sharp corners that control abrasion (Manga et al., 2011). The
502 Avellino experiments showed the most evidence for splitting during milling, with the clast number
503 almost doubling (from 7 to 12 clasts) in one sub-sample (Av32a AD sample; Table 1). In these
504 experiments, the large proportion of material in the -2φ grain size (expected for splitting of -3φ grains),
505 as well as the abundance of ash in the intermediate grainsizes (-1φ to 2φ; Fig. 5), suggest that splitting
506 was a dominant, rather than occasional, process. The post-abrasion range in FF values and the
507 frequency of outlying FF values (Fig. 7) also provide evidence of splitting. The HD sub-sample of
508 Av33a provides a particularly striking example of the hypothesis that splitting of Avellino clasts aids
509 efficient ash generation. Here the largest clast completely disintegrated (extensive splitting), which
510 increased ash generation across the intermediate (-1φ to 2φ) grain sizes compared to the other Avellino
511 HD subsamples (Fig. 6b).

512 Our data further suggest that internal weaknesses that encourage splitting (such as large vesicles or
513 cavities formed by decarbonation) are exploited rapidly, so that over time, splitting becomes far less
514 common. This means that after long milling times (as in Manga et al., 2011), rounding of all fragments
515 makes the products of splitting indistinguishable from clasts that experienced only abrasion. If we had
516 used longer milling times for our experiments, the effects of splitting may have been masked by
517 continual abrasion of the split clasts. In a natural setting, initial splitting of clasts may add to the early
518 maximum in ash production by comminution between clasts as the splitting exposes rough surfaces that
519 are readily available for progressive abrasion (Dufek and Manga, 2008).

520 **5.3 Enhanced ash production due to the interaction of pyroclasts with variable resistance**

521 A recent study of PDC deposits from Tungurahua volcano in Ecuador (Bernard and Le Pennec, 2016)
522 found that old lava clasts incorporated within the flow caused early splitting of pristine juvenile
523 components (termed 'grinding'), due to the increased strength of the lava. This interpretation is
524 supported by our supplementary Avellino experiment, Av3AG (Table 1). Here adding an agate ball to
525 the grinding jar (analogous to adding a resistant lithology) enhanced ash production, particularly in the
526 intermediate grain size fractions (Fig. 6c). The study of the Tungurahua PDC deposits further indicates
527 that initial splitting (or 'grinding') of the juvenile clasts generates a 'milling factory' that produces small

juvenile fragments that are available to abrade (Bernard and Le Pennec, 2016). This is consistent with our results showing that initial breakage of clasts (-3 or -2φ) will enhance further ash production by abrasion (see section 5.2).

Taken together, these observations suggest that the presence (in PDCs) of mixed lithologies with different strengths encourages a productive milling factory, making block-and-ash flows prone to ash production. Large volume PDCs (ignimbrites), in contrast, tend to be pumice-dominated, with minor contributions of lithic fragments (e.g., Sparks et al., 1973). Therefore, enhanced splitting and abrasion due to grinding by a resistant lithic component could be less important in pumice-dominated flows than in flows with a higher lithic content. Our experiments also suggest, however, that even a small proportion of lithics will enhance ash production.

5.4 Controls of the starting materials texture on the characteristics of the ash produced

5.4.1 Ash grainsize

The fine modes of GSDs produced by abrasion experiments are 5φ for Avellino and 4φ for Fuego. The difference in the fine modes reflects the different starting materials used. Thin vesicle walls provide preferential places for rocks to fracture (e.g., Heap et al., 2014). If abrasion is caused by breakage of juvenile clasts at vesicle walls, the size of the ash generated will be limited by the bubble wall thickness, which explains the coarser mode (4φ) of the ash generated by the (thick walled) Fuego experiments. Fracturing and breakage of volcanic rocks can also occur in the absence of vesicles. In this case it is likely that the high crystallinity (~40%) of the Fuego groundmass will prevent extensive breakage of particles into smaller grainsizes as microlites likely increase the strength of the groundmass (Heap et al., 2016).

5.4.2 Ash componentry

The experimental GSDs show that the crystallinity and vesicularity of the starting material exert strong controls on the amount and size of ash generated by abrasion. The starting material properties also strongly influence the physical attributes of the resulting ash. For example, the abundance of vesicular ash grains is controlled by the minimum vesicle size in the starting material (Liu et al., 2015b). For this

554 reason, the Fuego 3φ (175-125 μm) ash lacks vesicular grains because the dominant vesicle size in
555 Fuego clasts is >100μm in diameter (Figs. 3 and 10). Avellino ash of the same grain size, in contrast,
556 contains a high proportion of vesicular grains because the average vesicle size in the pumice is smaller
557 than the ash size (Fig. 10).

558 The crystal content of the ash reflects the crystallinity of the starting materials. The Fuego 3φ ash
559 comprises >90% crystalline particles (free crystals and crystal-rich groundmass) compared to ~70%
560 crystalline particles in the Avellino 3φ ash (mostly phenocrysts with or without attached matrix).
561 However, the proportion of free crystals in the Avellino ash is higher than in the Fuego ash. This could
562 be the result of efficient liberation of crystals from the surrounding matrix during abrasion (Fig. 12)
563 and/or breakage of larger crystals along cleavage planes (Jones et al., 2016). Without analysing ash
564 componentry in other grain size fractions, however, it is not possible to determine the primary origin of
565 the free crystal fragments or the abundance of free crystals in the whole ash sample.

566 Experimental milling (abrasion) can also reduce the amount of matrix adhered to crystals (the
567 Adherence Factor, AF) of ash particles (Jones et al., 2016). The Adherence Factor trends shown in
568 Figure 12 clearly distinguish the Fuego ash (higher proportion of high AF) from the Avellino ash
569 (mostly low AF values). The different AF trends reflect different textures in the starting material, most
570 importantly, the vesicularity of the matrix surrounding the crystals. For example, the low vesicularity
571 and thick bubble walls in the Fuego clasts (Fig. 3) means the maximum amount of matrix that can be
572 attached to a crystalline ash particle is greater than for the Avellino pumice, thus explaining the higher
573 AF values. Another factor that could influence the AF is the variable thermal contraction of
574 components during cooling which can create curvilinear fractures separating crystals from the glass
575 (Andronico and Cioni, 2002). These fractures would help liberate crystals from the melt increasing the
576 occurrence of crystals with a minor amount of attached matrix and therefore a low AF.

577 5.4.3 Ash Shape

578 It has been suggested that co-PDC ash might have more uniform shapes than fall ash due to the
579 smoothing of grain boundaries by abrasion (Liu et al., 2015a; Taddeucci and Palladino, 2002). This was

580 illustrated by Tambora co-PDC ash, which had a higher convexity (CVX) than fall ash with the same
581 solidity (SLD), consistent with an abrasion-induced decrease of the roughness of grain perimeters
582 during transport within PDCs (Liu et al., 2015a). The analysis was based, however, on a limited number
583 of 2φ (350-500μm) ash particles (Maria and Carey, 2007). Here we assess the extent to which fine-
584 grained ash generated by experimental abrasion records similarly high convexity values as the result of
585 rounding.

586 The highest density of data points for both Avellino and Fuego ash (the 50% contour encloses
587 approximately half of the data) plot with CVX and SLD >0.9 (Fig. 8). However, the Avellino projected
588 area shape analysis extends to lower CVX and SLD values (~0.87) than for Fuego ash (~0.9). This
589 difference reflects the componentry, with the vesicular grains in the Avellino ash having low CVX and
590 SLD. The different SLD and CVX ranges for Avellino and Fuego ash are more pronounced in the
591 cross-sectional shape analysis, shown in Figure 9. This demonstrates the ability of this method to
592 distinguish particles characterised by contrasting internal structures rather than using the projected
593 shape (Morphologi). We therefore conclude that not all ash formed by abrasion will record high
594 convexity values, particularly when grains are vesicular. These data also show that the morphological
595 changes undergone by lapilli and ash can be decoupled during milling in PDCs, with larger clasts
596 rounding but newly generated ash having highly irregular shapes. This is particularly apparent in the
597 Avellino experiments where lapilli clasts exhibit pronounced rounding (Fig. 7) but the ash generated
598 preserves the initial textures of the starting material (high vesicularity) resulting in extremely irregular
599 ash shapes (Fig. 9).

600 Shape and componentry have been linked using BSE images (Liu et al., 2015a); here we extend this to
601 projected area (Morphologi) images using simple componentry classifications that allowed us to relate
602 CVX and SLD shape parameters to ash componentry in the 3φ grainsize (Fig. 8). We can also use the
603 shape data to infer componentry from CVX-SLD plots (Fig. S2). From these data, it appears that the
604 vesicular clast content of the 4φ Avellino ash is higher than for the 3φ grainsize. This is contrary to
605 expectation, as the proportion of vesicular fragments typically decreases with grain size when the
606 bubble diameter approaches the average particle diameter. It is possible that this effect is not apparent

607 between 3 and 4φ due to the small modal vesicle size in the Avellino pumice and/or there may be fewer
608 free crystal grains in the 4φ size fraction. This comparison, and our interpretation of the results,
609 demonstrates the dependency of componentry on grain size and builds on the conclusions of Liu et al.
610 (2015b) that multiple grain sizes should be characterised for shape and componentry where feasible.
611 Furthermore, the differences between results from the two methods of shape analysis - BSE and
612 Morphologi - demonstrate that caution is required when comparing datasets collected by different
613 methods and protocols (e.g. Liu et al., 2015a).

614 **5.5 Comparison between experimental results and natural settings**

615 The shapes of ash particles produced by experimental and natural processes are not identical. Ash from
616 a Fuego pyroclastic surge deposit, for example, has higher values of solidity and convexity than the
617 experimentally generated ash (Fig. 11). This is likely explained by the short duration of our experiments,
618 the experimental conditions of room (rather than high) temperature and the uniformity (in size and
619 density) of the starting material. Interestingly, although the experimental ash does not exactly replicate
620 the natural PDC-surge ash properties (Fig. 11b), the morphologies of the two ash samples are more
621 similar to each other than to ash produced by primary fragmentation (fall ash from Fuego 2016), which
622 records a much larger range of CVX and SLD values (Fig. 11a). This suggests that the abrasion
623 experiments have successfully produced ash with shapes that replicate the shape characteristics of
624 naturally abraded ash.

625 Ash from the PDC matrix of the Avellino EU3pf deposit also has higher values of SLD and CVX than
626 the experimental products (Fig. 11c), consistent with more extensive milling in a PDC compared to the
627 short experimental milling times. An additional difference between the natural and experimental
628 Avellino ash samples is the large lithic component of the natural PDC-matrix ash (Fig. 11f). These
629 fragments of lavas, skarn and wall rocks provide evidence for the presence and abrasion of resistant
630 lithologies during PDC emplacement.

631 The most compelling similarities between the natural and experimental samples, are the Adherence
632 Factor trends (Fig. 12), which closely match each other for both Fuego and Avellino. Moreover, the

633 AF trend of the intermediate Soufriere Hills pumice (intermediate in both vesicularity and crystallinity)
634 demonstrates that AF can be used to distinguish abrasion products that have formed from starting
635 materials with different physical properties, as the efficiency of matrix stripping is dependent on the
636 vesicularity and microlite content of the matrix. Finally, experiments on Avellino pumice show that
637 extensive abrasion within a PDC can produce abundant fine ash (mean size ~30-60μm). In natural
638 mixed fallout deposits (deposits containing both fall and material generated in the PDC), the GSDs can
639 be either uni- or bimodal depending on factors such as the distance from source and the positions relative
640 to the primary dispersion axis (Engwell and Eychenne, 2016). With increasing distance from the vent,
641 the GSD becomes unimodal converging on the fine mode as the size of the primary fall ash approaches
642 the grain size of the ash generated by secondary processes, such as abrasion in PDCs. The fine mode
643 of the GSDs produced by the abrasion experiments are 5φ for the Avellino and 4φ for the Fuego. This
644 size range not only overlaps with natural co-PDC ash (mean of the fine subpopulations of bimodal
645 samples), but may also explain the variations in co-PDC ash size from different source volcanoes. For
646 example co-PDC (blast) ash from Mount St Helens has a mean size of 5-6φ, which contrasts with the
647 4φ mean of the highly crystalline Fuego samples (Engwell and Eychenne, 2016).

648 The amount and size distribution of fine ash will be a key factor in the development of a co-PDC plume,
649 which can transport ash to the atmosphere (Woods and Wohletz, 1991). Numerous co-PDC layers
650 associated with large pumice-rich PDCs are found in the stratigraphic record, including eruptions from
651 Somma Vesuvius and the nearby Phlegrean fields (e.g., Engwell et al., 2014; Sulpizio et al., 2008).
652 These deposits support our finding that crystal-poor pumice clasts, such as those that comprise the
653 Avellino deposit, are susceptible to extensive secondary fragmentation and co-PDC plume formation,
654 which can greatly enhance ultra-distal transport of fine ash.

655 In contrast, discrete co-PDC ash layers from block and ash flows, such as from Fuego, are much less
656 common. Evidence of ash generation in such flows comes mainly from observation of the bimodality
657 of the fallout deposit grainsize (e.g., Engwell and Eychenne, 2016; Eychenne et al., 2012). Nonetheless,
658 abrasion within block and ash flows can generate sufficient fine ash to increase their mobility, thus
659 elevating their risk factor (Cole et al., 1998; Fujii and Nakada, 1999). However, we suggest that the

660 elevated groundmass crystallinity of constituent clasts will ultimately limit the smallest grain size that
661 can be produced by abrasion, and the efficiency of ash generation. Therefore, crystal-rich material in
662 block and ash flows produced by microlite-rich magma is less likely to produce a co-PDC plume with
663 a large dispersal extent than low density, low crystallinity pumice flows.

664 **6. Conclusions**

665 Previous abrasion experiments have found that low density (high vesicularity) pyroclasts generate more
666 ash than high density (low vesicularity) pyroclasts. Although generally true in our experiments, we
667 found that the pyroclast density (vesicularity) alone is insufficient to predict how pyroclastic material
668 will react to abrasion. The ash-generating potential of pyroclastic material is also controlled by the
669 crystal content, as well as heterogeneities in bubble and crystal textures. Two key relationships were
670 observed between the amount of ash generated and the crystal content. Firstly, experiments on
671 microlite-rich pyroclasts from Fuego volcano showed that increasing the heterogeneity of the crystal
672 population of a (relatively) low-density clast renders it more resistant to abrasion than a high-density
673 clast with more uniform phenocryst and groundmass characteristics. Secondly, details of both the
674 vesicle and crystal content of pyroclasts can encourage clasts to split rather than abrade. Increasing the
675 frequency of clast splitting enhances the ash-generating potential because splitting creates new irregular
676 surfaces that are susceptible to abrasion.

677 The vesicularity and crystal content of the starting material strongly influences the properties of the ash
678 generated by abrasion, in addition to the amount of ash generated. Critically, high microlite crystallinity
679 limits the generation of very fine ash, as shown by the lower abundance and larger size of the ash
680 generated in the crystal-rich Fuego experiments (4φ) compared to the crystal-poor Avellino experiments
681 (5φ). The vesicularity and crystal content of pyroclasts also controls the componentry of ash generated
682 by abrasion, which in turn influences ash shape and, by extension, elutriation and transport (settling)
683 properties. Co-PDC ash with mixed componentry, (e.g. mainly free crystals and highly vesicular ash),
684 poses a challenge to dispersion modelling as typically a single density measurement is required for
685 dispersion models (e.g., Mastin et al., 2010; Witham et al., 2007). Moreover, the vesicular glass
686 particles will be preferentially elutriated compared to crystals of the same size, due to their low density,

687 altering the componentry of the ash that is dispersed from the PDC to the atmosphere as evidenced by
688 crystal-enriched ignimbrite deposits (Sparks and Walker, 1977).

689 Abrasion can also alter ash shape. Ash produced in a PDC-surge deposit from Fuego preserves grains
690 with reduced roughness compared to natural fall Fuego ash (e.g., Liu et al., 2015a). However, we did
691 not detect reduced roughness of ash generated by abrasion of the highly vesicular Avellino ash. The
692 Adherence Factor, which quantifies the amount of matrix adhered to (micro)phenocrysts, is most
693 effective for distinguishing ash that has undergone different degrees of abrasion (Jones et al., 2016) We
694 also have shown that AF can clearly distinguish ash from different starting materials due to the
695 maximum amount of matrix that can be attached to a crystal which is determined by the vesicularity of
696 the matrix. Efficient abrasion strips the matrix from ash grains and this process is more efficient in high
697 vesicularity materials with low-crystallinity vesicular groundmass such as the Avellino pumice.

698 When compared to natural samples, the experimentally generated ash differed somewhat from the
699 natural PDC-surge and PDC-matrix ash samples due to differences in abrasion conditions and the
700 presence of xenoliths. However, the fine modes of the grainsize distributions produced by the milling
701 are similar to the fine modal grainsizes measured in natural fallout deposits where co-PDC ash has been
702 recorded (Engwell and Eychenne, 2016). This suggests the experimental abrasion is effectively
703 replicating the natural process.

704 **Acknowledgements**

705 This work was completed with support from the AXA Research Fund. We thank B. Voarino and J.
706 Hanson for their sampling of the Pomici de Avellino deposit and E. Liu for sampling the surge and fall
707 Fuego ash. We also thank S. Kearns, B. Buse and K. McNamara for their support during SEM and
708 image analysis. Further thanks extend to L. Gurioli and the volcanology group at Laboratoire Magmas
709 et Volcans for their help with the Morphologi OPA measurements. Finally we thank J. Gardner for the
710 editorial handling of the manuscript, and R. Cioni and U. Kueppers for constructive reviews that greatly
711 improved the quality of this manuscript.

712

Figures, captions and tables (for high quality figures please see separately uploaded pdfs):

Figure 1: Density histograms of the -3φ juvenile populations of both Fuego (a) and Avellino (b). The bins are 0.1gcm-3 intervals and the number of clasts measured is denoted by 'n'. The diamond, circle and triangle symbols indicate the mean density of the low density (LD), average density (AD) and high density (HD) sub-samples, respectively. a.) FUE2a: filled black symbols, FUE3a: white symbols and FUE5a: open black symbols. b.) Av31a: filled black symbols, Av32a: white symbols and Av33a: open black symbols. The upper x-axis is the vesicularity (%) calculated using the DRE densities (Houghton and Wilson, 1989). See Table 1 for the list of samples and experiments.

Figure 2: Summary of abrasion experiment apparatus. The Retsch Planetary Ball Mill PM100 consists of a rotating basal plate and agate-lined 7.5cm diameter milling jar which contains the sample. The rotation rate and milling duration are input by the user. The sample is retrieved after milling using a clean fine brush and stored in a tightly sealed sample bag. Between all samples and sub-samples, the milling jar is cleaned with clean silicon sand, milled for 4 minutes.

Figure 3: Textural differences in vesicle populations between Fuego sub-samples from BSE-SEM images. a.) Low density clast, b.) low density clast with large glomercrysts and increased microlite content, c.) average density clast and d.) high density clast. The boxes below contain the density of individual clasts and the results of the two methods of quantifying vesicularity. The VF values are lower than the VD values for the LD and HD clasts as the 2D imaging tends to exclude the largest vesicles. e.) to h.) are the vesicle size distributions of the e.), f.) low Density, g.) average density and h.) high density clasts. Bin sizes are in phi increments.

Figure 4: Irregularities in vesicularity and crystal content within Avellino pumice. a.) An example of a localised area of dense microlite rich melt. b.) A close-up view of the boundary between the two zones of crystal and vesicle content. c.) An image of an embedded fragment of thermally recrystallised limestone with large surrounding vesicle likely due to thermal decomposition of the carbonate minerals.

737 Figure 5: Grain size histograms after 4 minutes of milling. The grey bar represents the starting grain
738 size. 'Expected trend' meaning, low density (high vesicularity) sub-samples generate more ash than
739 high density (low vesicularity) sub-samples.

740 Figure 6: Total grainsize distributions of all samples following 4 minutes of abrasion in a planetary ball
741 mill. The starting grainsize is represented by the y-axis (-3φ). a.) TGSDs generated following three
742 abrasion experiments using Fuego juveniles. Different lines styles correspond to different density sub-
743 samples. b.) The GSDs generated following the abrasion experiments using the Avellino juveniles. The
744 colours correspond to the histograms in Figure 5. c.) TSGDs of supplementary Avellino experiments.
745 *Av31b used a -2φ starting grainsize fraction.

746 Figure 7: Box plots of form factor (FF) measurements for *all* milling experiments of Fuego and Avellino
747 material. Numbered boxes indicate clast count for all three experiments before (-3φ) and after milling
748 (-3 and -2φ). Black forms at top are examples of binary images used to measure the FF using ImageJ.
749 The examples are from the F2a AD and Av33a HD sub-samples. Small black boxes indicate outliers,
750 which only occur in the Avellino data.

751 Figure 8: Morphologi shape analysis of F3a and Av31a AD 3φ ash using shape factors solidity and
752 convexity. a.) Fuego ash analysis. b.) Avellino ash analysis. 'n' denotes the grain count. The points
753 are translucent, so the stronger colour indicates more points. The contours are of the kernel density and
754 are labelled at with the proportion of points they enclose. c.) and d.) are plots of randomly selected
755 500 grains from the Fuego (c) and Avellino (d) ash that have been split into different components.

756 Figure 9: Results of ImageJ and BSE image analysis of a.) F3a and b.) Av31a 3φ AD sample ash at
757 high image resolution (~ 1560 pixels/mm). Scatter plots of solidity and convexity shown. The contours
758 and dashed boxes are where the Morphologi results of the same sample plot (Figure 8). Binary images
759 of ash grains are shown along axes to demonstrate range in shape parameters.

760 Figure 10: Componentry analysis from BSE images of a.) F3a and b.) Av31a 3φ (125-180 μm) ash.
761 The glass category refers to particles that are almost entirely vesicle-free and microlite-free glass.
762 Images of each component type can be found in Figure S3.

Figure 11: Cross-sectional shape analysis of natural and experimental ash samples. a.) to c.) Kernel density contours of solidity and convexity of a.) natural fall ash from a paroxysm of Volcan de Fuego in 2016; b.) natural Fuego PDC-surge ash from 2012 (E. Liu, *personal comm.*); c.) natural PDC-matrix ash from the EU3pf deposit. The contour intervals correspond to those in Figure 8 and are labelled with the proportion of data they enclose. The shaded contours at the same intervals represent the Fuego F3a (red) and Avellino Av31a (blue) SLD and CVX data of experimental ash at reduced resolution (~390 pixels/mm). d.) and e). are cumulative frequency plots of convexity and solidity. The dashed lines correspond to the natural samples which record a higher proportion of high CVX and SLD values than the equivalent experimental ash sample. f.) BSE image of the natural Avellino PDC-matrix ash, highlighting the large lithic component.

Figure 12: Adherence factor plot of the Avellino and Fuego milling experiments, the natural PDC-surge and matrix ash samples and the data from two milling experiments carried out by Jones et al., (2016) using Soufriere Hills Volcano (SHV) pumice; the latter were shorter duration experiments but six agate milling balls used so we assume similar milling efficiencies. Adherence Factor is plotted cumulatively so that each point indicates the percentage of crystals with that AF value or less. AF values close to 1 represent a large amount of attached matrix.

Table 1 – Abrasion experiments and summary: sample names, experiment conditions and subsequent analysis. The 'sample characterisation' column lists the clasts that were mounted for vesicularity and crystal content assessment. Some of the sample characterisation was before milling (BM clasts) and some was done after milling (AM clasts). The clast shape analysis column signifies the samples where the larger clasts were photographed, and their shape analysed. All experiments started with -3φ clasts solely and lasted 4 minutes, apart from the two additional Avellino experiments Av31b and Av3AG. Av31b used starting material in the -2φ fraction and was milled for 5 minutes. Av3AG included one agate ball as a proxy for a lithic component. FUE003 are average density juveniles from the Fuego PDC deposit not used in the abrasion experiments. AV-16-01 is an Avellino fall pumice, also not used in the abrasion experiments (Voarino, 2016).

Sample Name	*Sub-Samples*	No. of clasts BM	No. of clasts AM (remaining in -3φ)	No. of clasts AM (in -3φ and -2φ)	Milling time (mins)	Rotation Rate (rpm)	Sample Characterisation	FOAMS	Clast Shape	Morphologi Analysis	BSE-SEM and ImageJ Analysis	Adherence Factor
FUE2a	LD	10	8	10	4	450	2 x clasts AM	2 x clast	✓		✓ 3φ	✓ 3φ
	AD	10	8	11	4	450			✓		✓ 3φ	✓ 3φ
	HD	10	9	12	4	450	1 x clast AM		✓		✓ 3φ	✓ 3φ
FUE3a	LD	10	4	9	4	450	1 x clast AM	1 x clast	✓	✓ 3φ, 4φ	✓ 3φ	
	AD	10	6	12	4	450	2 x clast AM	2 x clast	✓	✓ 3φ, 4φ	✓ 3φ	
	HD	10	8	10	4	450		1 x clast	✓	✓ 3φ, 4φ	✓ 3φ	
FUE5a	LD	10	7	11	4	450	1 x clast AM	1 x clast	✓			
	AD	10	5	13	4	450			✓			
	HD	10	4	13	4	450	1 x clast AM	1 x clast	✓			
FUE003							2 x clast BM	1 x clast				
Av31a	LD	7	1	6	4	450	3 x clasts AM		✓	✓ 3φ, 4φ	✓ 3φ	✓ 3φ
	AD	7	3	7	4	450	2 x clasts AM		✓	✓ 3φ, 4φ	✓ 3φ	✓ 3φ
	HD	7	1	10	4	450	4 x clasts AM		✓	✓ 3φ, 4φ	✓ 3φ	✓ 3φ
Av32a	LD	8*	1	12	4	450			✓			
	AD	7	2	10	4	450	1 x clast AM		✓			
	HD	7	3	7	4	450			✓			
Av33a	LD	7	1	7	4	450			✓		✓ 3φ	
	AD	7	2	7	4	450			✓		✓ 3φ	
	HD	7	1	9	4	450	1 x clast AM		✓		✓ 3φ	
Av31b	LD	40		15	5	450						
	AD	40		38	5	450						
	HD	40		42	5	450						
Av3AG	AD	7	5	9	4	450			✓		✓ 3φ	
AV-16-01	*Avellino fall pumice not used in abrasion experiments, only vesicularity characterisation***						2 x clast	1 x clast				

* There were 7 clasts but one broke during loading prior to milling

** Imaging and FOAMS analysis carried out by Voarino, (2016).

Table 2 – Shape parameters and definitions. This table only highlights key parameters used in this study, see Liu et al., (2015) for a comprehensive summary of shape factors and uses.

Shape Parameter	Abbreviation	Formula	Symbols	Sensitivity	Alternative nomenclature	References
Form Factor	FF	$4\pi A_P / P_P^2$	A_P = area of particle P_P = perimeter of particle	Form and roughness	Sphericity, Roundness, Circularity, HS Circularity, Shape Factor, Cox circularity	Liu et al., 2016 and references within
Solidity	SLD	A_P/A_{CH}	A_P = area of particle A_{CH} = area of convex hull	Roughness (morphological)		Liu et al., 2016
Convexity	CVX	P_{CH}/P_P	P_{CH} = perimeter of convex hull P_P = perimeter of particle	Roughness (textural)	Roughness	Liu et al., 2016
Adherence Factor	AF	A_M/A_M+A_C	A_M = area of attached matrix A_C = area of crystal	Amount of attached matrix	Abrasion index (A_P/A_M)	Jones et al., 2016, Freundt & Schminke, 1992

References

Andronico, D., Cioni, R., 2002. Contrasting styles of Mount Vesuvius activity in the period between the Avellino and Pompeii Plinian eruptions, and some implications for assessment of future hazards. Bull. Volcanol. 64, 372–391. doi:10.1007/s00445-002-0215-4

Balcone-Boissard, H., Boudon, G., Ucciani, G., Villemant, B., Cioni, R., Civetta, L., Orsi, G., 2012. Magma degassing and eruption dynamics of the Avellino pumice Plinian eruption of Somma-Vesuvius (Italy). Comparison with the Pompeii eruption. Earth Planet. Sci. Lett. 331–332, 257–268. doi:10.1016/j.epsl.2012.03.011

Berlo, K., Stix, J., Roggensack, K., Ghaleb, B., 2012. A tale of two magmas, Fuego, Guatemala. Bull. Volcanol. 74, 377–390. doi:10.1007/s00445-011-0530-8

Bernard, J., Le Pennec, J.L., 2016. The milling factory: Componentry-dependent fragmentation and fines production in pyroclastic flows. Geology 44, 907–910. doi:10.1130/G38198.1

Bindeman, I.N., 2005. Fragmentation phenomena in populations of magmatic crystals. Am. Mineral. 90, 1801–1815. doi:10.2138/am.2005.1645

Chesner, C.A., Rose, W.I., 1984. Geochemistry and evolution of the Fuego volcanic complex, Guatemala. J. Volcanol. Geotherm. Res. 21, 25–44. doi:10.1016/0377-0273(84)90014-3

Chigna, G., Giron, J., Barrios, E., Calderas, A., Cornejo, J., 2012. Reporte de la erupcion del volcan fuego 13 septiembre 2012.

Cioni, R., Santacroce, R., Sbrana, A., 1999. Pyroclastic deposits as a guide for reconstructing the multi-stage evolution of the Somma-Vesuvius Caldera. Bull. Volcanol. 61, 207–222.

Cole, P.D., Calder, E.S., Druitt, T.H., Hoblitt, R., Robertson, R., Sparks, R.S.J., 1998. Pyroclastic flows generated by gravitational instability of the 1996-97 lava dome of Soufriere Hills Volcano, Montserrat. Geophys. Res. Lett. 25, 3425–3428.

Cole, P.D., Calder, E.S., Sparks, R.S.J., Clarke, A.B., Druitt, T.H., Young, S.R., Herd, R.A., Harford,

C.L., Norton, G.E., 2002. Deposits from dome-collapse and fountain-collapse pyroclastic flows at Soufrière Hills Volcano, Montserrat. Geol. Soc. London, Mem. 21, 231 LP-262.

Coltelli, M., Miraglia, L., Scollo, S., 2008. Characterization of shape and terminal velocity of tephra particles erupted during the 2002 eruption of Etna volcano, Italy. Bull. Volcanol. 70, 1103–1112. doi:10.1007/s00445-007-0192-8

Dufek, J., Manga, M., 2008. In situ production of ash in pyroclastic flows. J. Geophys. Res. Earth 113. doi:10.1029/2007jb005555

Dufek, J., Manga, M., Patel, A., 2012. Granular disruption during explosive volcanic eruptions. Nat. Geosci. 5, 561–564. doi:10.1038/ngeo1524

Durant, A.J., Rose, W.I., 2009. Sedimentological constraints on hydrometeor-enhanced particle deposition: 1992 Eruptions of Crater Peak, Alaska. J. Volcanol. Geotherm. Res. 186, 40–59. doi:10.1016/j.jvolgeores.2009.02.004

Engwell, S., Eychenne, J., 2016. Chapter 4 – Contribution of Fine Ash to the Atmosphere From Plumes Associated With Pyroclastic Density Currents, in: Volcanic Ash. pp. 67–85. doi:10.1016/B978-0-08-100405-0.00007-0

Engwell, S.L., Sparks, R.S.J., Carey, S., 2014. Physical characteristics of tephra layers in the deep sea realm: the Campanian Ignimbrite eruption. Mar. Tephrochronology 398, 47–64. doi:10.1144/SP398.7

Engwell, S.L., Vitturi, M.D., Ongaro, T.E., Neri, A., 2016. Insights into the formation and dynamics of coignimbrite plumes from one-dimensional models. J. Geophys. Res. Earth 121, 4211–4231. doi:10.1002/2016jb012793

Eychenne, J., Le Pennec, J.L., Troncoso, L., Gouhier, M., Nedelec, J.M., 2012. Causes and consequences of bimodal grain-size distribution of tephra fall deposited during the August 2006 Tungurahua eruption (Ecuador). Bull. Volcanol. 74, 187–205. doi:10.1007/s00445-011-0517-5

Ferreira, T., Rasband, W., 2012. ImageJ User Guide IJ 1.46r. IJ 1.46r 185. doi:10.1038/nmeth.2019

Freundt, A., Schmincke, H.U., 1992. Abrasion in pyroclastic flows. Geol. Rundschau 81, 383–389. doi:10.1007/bf01828605

Fujii, T., Nakada, S., 1999. The 15 September 1991 pyroclastic flows at Unzen Volcano (Japan): a flow model for associated ash-cloud surges. J. Volcanol. Geotherm. Res. 89, 159–172. doi:10.1016/S0377-0273(98)00130-9

Gardner, C.A., Cashman, K. V., Neal, C.A., 1998. Tephra-fall deposits from the 1992 eruption of Crater Peak, Alaska: implications of clast textures for eruptive processes. Bull. Volcanol. 59, 537–555. doi:10.1007/s004450050208

Gonnermann, H.M., 2015. Magma Fragmentation. Annu. Rev. Earth Planet. Sci. Vol 43 43, 431–458. doi:10.1146/annurev-earth-060614-105206

Gravina, T., Lirer, L., Marzocchella, A., Petrosino, P., Salatino, P., 2004. Fluidization and attrition of pyroclastic granular solids. J. Volcanol. Geotherm. Res. 138, 27–42. doi:10.1016/j.jvolgeores.2004.06.005

Gudmundsson, M.T., Thordarson, T., Hoskuldsson, A., Larsen, G., Bjornsson, H., Prata, F.J., Oddsson, B., Magnusson, E., Hognadottir, T., Petersen, G.N., Hayward, C.L., Stevenson, J.A., Jonsdottir, I., 2012. Ash generation and distribution from the April-May 2010 eruption of Eyjafjallajokull, Iceland. Sci. Rep. 2. doi:10.1038/srep00572

Heap, M.J., Wadsworth, F.B., Xu, T., Chen, C. feng, Tang, C., 2016. The strength of heterogeneous volcanic rocks: A 2D approximation. J. Volcanol. Geotherm. Res. 319, 1–11. doi:10.1016/j.jvolgeores.2016.03.013

Heap, M.J., Xu, T., Chen, C., 2014. The influence of porosity and vesicle size on the brittle strength of volcanic rocks and magma. Bull. Volcanol. 76, 1–15.

Horwell, C.J., 2007. Grain-size analysis of volcanic ash for the rapid assessment of respiratory health hazard. J. Environ. Monit. 9, 1107–1115. doi:10.1039/010583p

Houghton, B.F., Wilson, C.J.N., 1989. A vesicularity index for pyroclastic rocks. Bull. Volcanol. 51,

451–462. doi:10.1007/bf01078811

Jolis, E.M., Troll, V.R., Harris, C., Freda, C., Gaeta, M., Orsi, G., Siebe, C., 2015. Skarn xenolith record crustal CO2 liberation during Pompeii and Pollena eruptions, Vesuvius volcanic system, central Italy. Chem. Geol. 415, 17–36. doi:10.1016/j.chemgeo.2015.09.003

Jones, T.J., McNamara, K., Eychenne, J., Rust, A.C., Cashman, K. V, Scheu, B., Edwards, R., 2016. Primary and secondary fragmentation of crystal bearing intermediate magma. J. Volcanol. Geotherm. Res. doi:10.1016/j.jvolgeores.2016.06.022

Kueppers, U., Putz, C., Spieler, O., Dingwell, D.B., 2012. Abrasion in pyroclastic density currents: Insights from tumbling experiments. Phys. Chem. Earth 45–46, 33–39. doi:10.1016/j.pce.2011.09.002

Leibrandt, S., Le Pennec, J.L., 2015. Towards fast and routine analyses of volcanic ash morphometry for eruption surveillance applications. J. Volcanol. Geotherm. Res. 297, 11–27. doi:10.1016/j.jvolgeores.2015.03.014

Liu, E.J., Cashman, K. V, Rust, A.C., 2015a. Optimising shape analysis to quantify volcanic ash morphology. GeoResJ 8, 14–30. doi:http://dx.doi.org/10.1016/j.grj.2015.09.001

Liu, E.J., Cashman, K. V, Rust, A.C., Gislason, S.R., 2015b. The role of bubbles in generating fine ash during hydromagmatic eruptions. Geology 43, 239–242. doi:10.1130/g36336.1

Lu, S.-Y., Mao, Q.-J., Peng, Z., Li, X.-D., Yan, J.-H., 2012. Simulation of ball motion and energy transfer in a planetary ball mill. Chinese Phys. B 21, 78201. doi:10.1088/1674-1056/21/7/078201

Manga, M., Patel, A., Dufek, J., 2011. Rounding of pumice clasts during transport: field measurements and laboratory studies. Bull. Volcanol. 73, 321–333. doi:10.1007/s00445-010-0411-6

Maria, A., Carey, S., 2007. Quantitative discrimination of magma fragmentation and pyroclastic transport processes using the fractal spectrum technique. J. Volcanol. Geotherm. Res. 161, 234–

246. doi:10.1016/j.jvolgeores.2006.12.006

Marti, A., Folch, A., Costa, A., Engwell, S., 2016. Reconstructing the plinian and co-ignimbrite sources of large volcanic eruptions: A novel approach for the Campanian Ignimbrite. Sci. Rep. 6, 11. doi:10.1038/srep21220

Mastin, L.G., Guffanti, M., Servranckx, R., Webley, P., Barsotti, S., Dean, K., Durant, A., Ewert, J.W., Neri, A., Rose, W.I., Schneider, D., Siebert, L., Stunder, B., Swanson, G., Tupper, A., Volentik, A., Waythomas, C.F., 2010. A multidisciplinary effort to assign realistic source parameters to models of volcanic ash-cloud transport and dispersion during eruptions (vol 188, pg 1, 2009). J. Volcanol. Geotherm. Res. 191, 245. doi:10.1016/j.jvolgeores.2009.10.013

Mio, H., Kano, J., Saito, F., Kaneko, K., 2002. Effects of rotational direction and rotation-to-revolution speed ratio in planetary ball milling. Mater. Sci. Eng. A 332, 75–80. doi:10.1016/S0921-5093(01)01718-X

Mueller, S.B., Lane, S.J., Kueppers, U., 2015. Lab-scale ash production by abrasion and collision experiments of porous volcanic samples. J. Volcanol. Geotherm. Res. 302, 163–172. doi:10.1016/j.jvolgeores.2015.07.013

Oppenheimer, J., Rust, A.C., Cashman, K. V., Sandnes, B., 2015. Gas migration regimes and outgassing in particle-rich suspensions. Front. Phys. 3, 1–13. doi:10.3389/fphy.2015.00060

Parmigiani, A., Faroughi, S., Huber, C., Bachmann, O., Su, Y., 2016. Bubble accumulation and its role in the evolution of magma reservoirs in the upper crust. Nature. doi:10.1038/nature17401

Parmigiani, A., Huber, C., Bachmann, O., Chopard, B., 2011. Pore-scale mass and reactant transport in multiphase porous media flows. J. Fluid Mech. 686, 40–76. doi:10.1017/jfm.2011.268

Rose, W.I., Durant, A.J., 2009. Fine ash content of explosive eruptions. J. Volcanol. Geotherm. Res. 186, 32–39. doi:10.1016/j.jvolgeores.2009.01.010

Rose, W.I., Self, S., Murrow, P.J., Bonadonna, C., Durant, A.J., Ernst, G.G.J., 2008. Nature and significance of small volume fall deposits at composite volcanoes: Insights from the October 14,

1974 Fuego eruption, Guatemala. Bull. Volcanol. 70, 1043–1067. doi:10.1007/s00445-007-0187-5

Rust, A.C., Cashman, K. V, 2011. Permeability controls on expansion and size distributions of pyroclasts. J. Geophys. Res. Earth 116. doi:10.1029/2011jb008494

Shea, T., Hammer, J.E., 2013. Kinetics of cooling- and decompression-induced crystallization in hydrous mafic-intermediate magmas. J. Volcanol. Geotherm. Res. 260, 127–145. doi:10.1016/j.jvolgeores.2013.04.018

Shea, T., Houghton, B.F., Gurioli, L., Cashman, K. V, Hammer, J.E., Hobden, B.J., 2010. Textural studies of vesicles in volcanic rocks: An integrated methodology. J. Volcanol. Geotherm. Res. 190, 271–289. doi:10.1016/j.jvolgeores.2009.12.003

Sottili, G., Taddeucci, J., Palladino, D.M., 2010. Constraints on magma-wall rock thermal interaction during explosive eruptions from textural analysis of cored bombs. J. Volcanol. Geotherm. Res. 192, 27–34. doi:10.1016/j.jvolgeores.2010.02.003

Sparks, R.S.J., Bursik, M.I., Carey, S., Gilbert, J., Glaze, L.., Sigurdsson, H., Woods, A.W., 1997. Volcanic plumes. Wiley.

Sparks, R.S.J., Self, S., Walker, G.P.L., 1973. Products of ignimbrite eruptions. Geology 1, 115–118. doi:10.1130/0091-7613(1973)1<115:POIE>2.0.CO;2

Sparks, R.S.J., Walker, G.P.L., 1977. SIGNIFICANCE OF VITRIC-ENRICHED AIR-FALL ASHES ASSOCIATED WITH CRYSTAL-ENRICHED IGNIMBRITES. J. Volcanol. Geotherm. Res. 2, 329–341. doi:10.1016/0377-0273(77)90019-1

Sulpizio, R., Bonasia, R., Dellino, P., Di Vito, M.A., La Volpe, L., Mele, D., Zanchetta, G., Sadori, L., 2008. Discriminating the long distance dispersal of fine ash from sustained columns or near ground ash clouds: The example of the Pomici di Avellino eruption (Somma-Vesuvius, Italy). J. Volcanol. Geotherm. Res. 177, 263–276. doi:10.1016/j.jvolgeores.2007.11.012

Sulpizio, R., Bonasia, R., Dellino, P., Mele, D., Di Vito, M.A., La Volpe, L., 2010a. The Pomici di

Avellino eruption of Somma-Vesuvius (3.9 ka BP). Part II: sedimentology and physical volcanology of pyroclastic density current deposits. Bull. Volcanol. 72, 559–577. doi:10.1007/s00445-009-0340-4

Sulpizio, R., Cioni, R., Di Vito, M.A., Mele, D., Bonasia, R., Dellino, P., 2010b. The Pomici di Avellino eruption of Somma-Vesuvius (3.9 ka bp). Part I: stratigraphy, compositional variability and eruptive dynamics. Bull. Volcanol. 72, 539–558. doi:10.1007/s00445-009-0339-x

Taddeucci, J., Palladino, D.M., 2002. Particle size-density relationships in pyroclastic deposits: inferences for emplacement processes. Bull. Volcanol. 64, 273–284. doi:10.1007/s00445-002-0205-6

Thomson, B.J., Bridges, N.T., Cohen, J., Hurowitz, J.A., Lennon, A., Paulsen, G., Zacny, K., 2013. Estimating rock compressive strength from Rock Abrasion Tool (RAT) grinds. J. Geophys. Res. Planets 118, 1233–1244.

Turcotte, D.L., 1986. Fractals and fragmentation. J. Geophys. Res. Earth Planets 91, 1921–1926. doi:10.1029/JB091iB02p01921

Voarino, B., 2016. Insights into fragmentation and column collapse triggers : A study of juvenile density and vesicle textures from the Pomici di Avellino steady plinian phase Brennus Voarino. MSc Thesis Sept. 2016. University of Bristol.

Walker, G.P.L., 1981. Generation and dispersal of fine ash and dust by volcanic eruptions. J. Volcanol. Geotherm. Res. 11, 81–92. doi:10.1016/0377-0273(81)90077-9

Wawersik, W.R., Fairhurst, C., 1970. A study of brittle rock fracture in laboratory compression experiments. Int. J. Rock Mech. Min. Sci. 7, 561–+. doi:10.1016/0148-9062(70)90007-0

Witham, C.S., Hort, M.C., Potts, R., Servranckx, R., Husson, P., Bonnardot, F., 2007. Comparison of VAAC atmospheric dispersion models using the 1 November 2004 Grimsvötn eruption. Meteorol. Appl. 14, 27–38. doi:10.1002/met.3

Woods, A.W., Wohletz, K., 1991. Dimensions and dynamics of co-ignimbrite eruption columns.

Nature 350, 225–227. doi:10.1038/350225a0

a.) Fuego

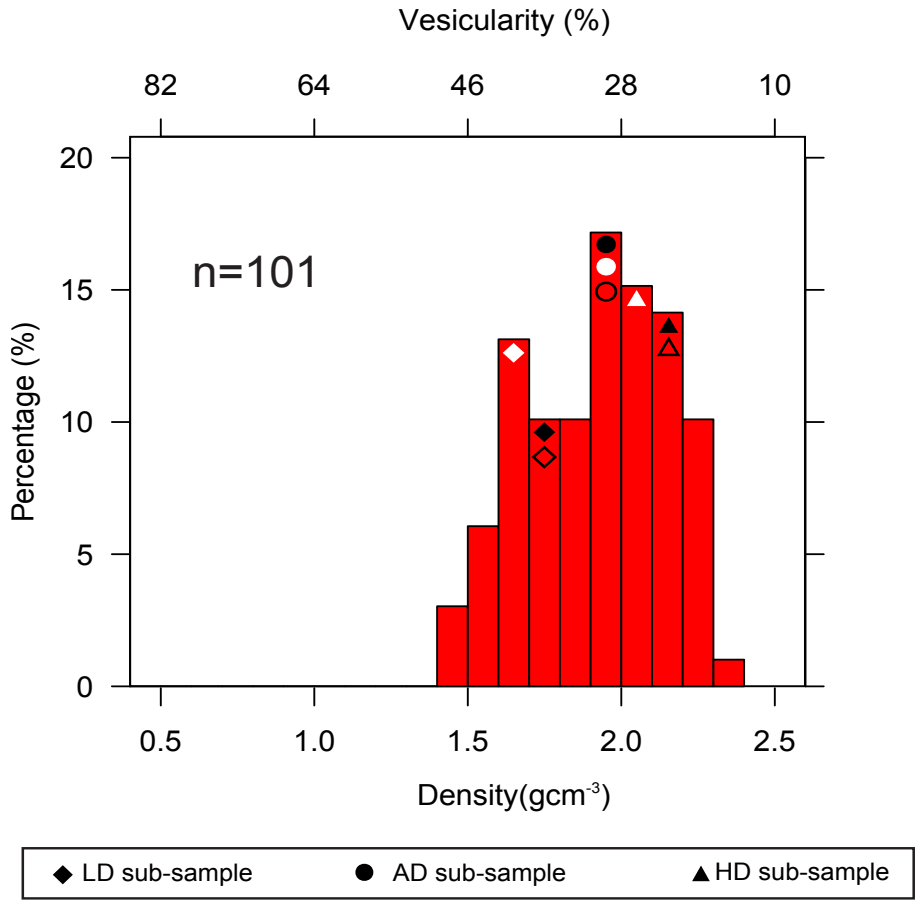

b.) Avellino

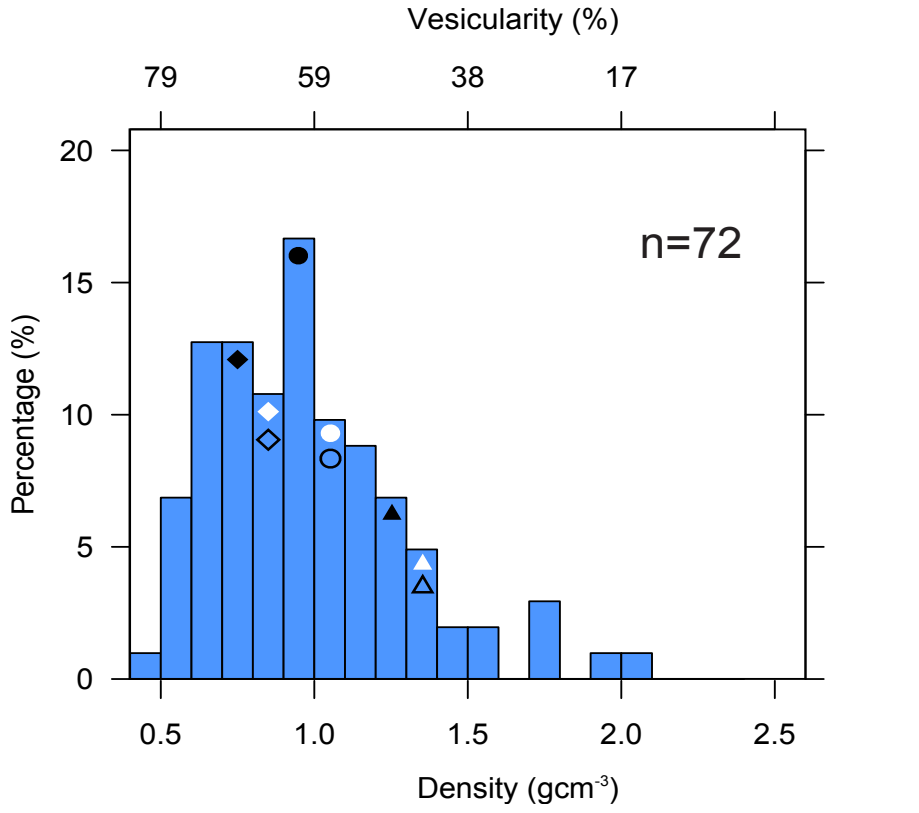

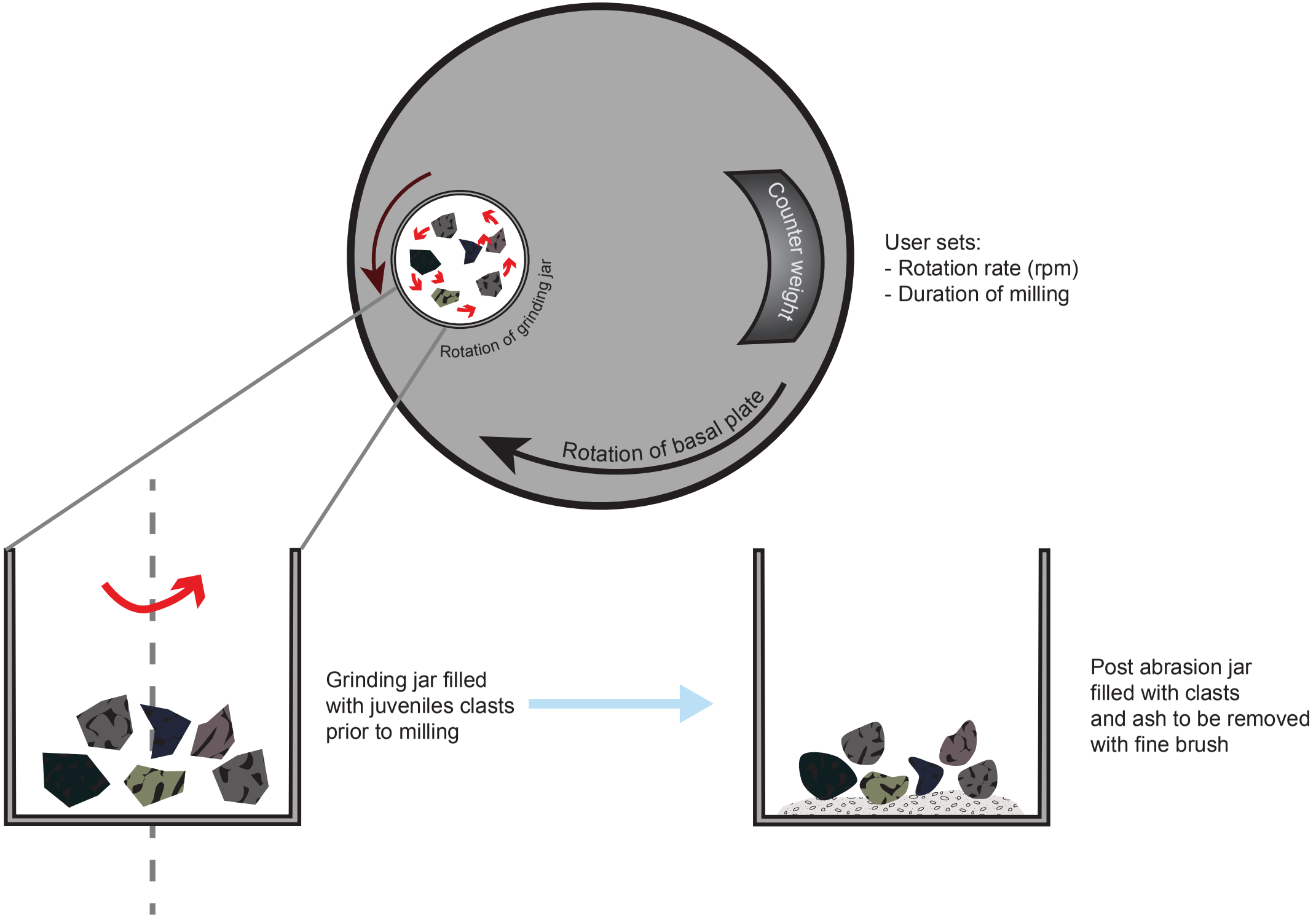
Counter weight
Rotation of grinding jar
Rotation of basal plate
User sets:
- Rotation rate (rpm)
- Duration of milling
Grinding jar filled
with juveniles clasts
prior to milling
Post abrasion jar
filled with clasts
and ash to be removed
with fine brush

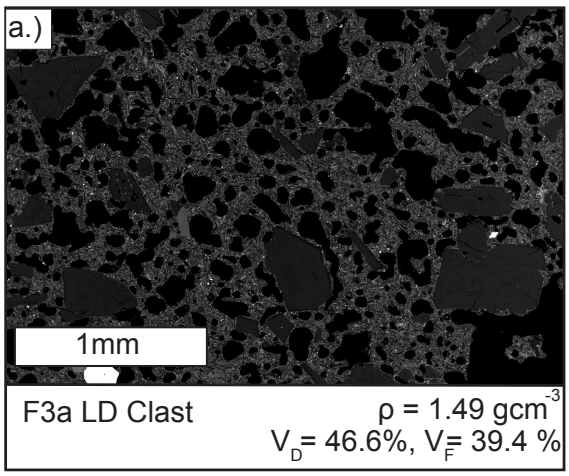
a.)
1mm
F3a LD Clast
ρ = 1.49 gcm-3
VD= 46.6%, VF= 39.4 %

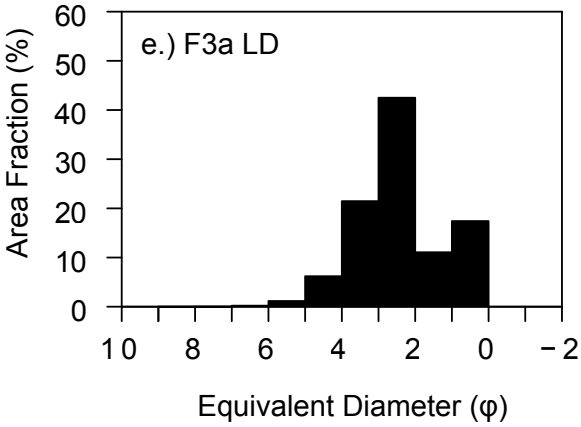
e.) F3a LD
Area Fraction (%)
60
50
40
30
20
10
0
10 8 6 4 2 0 −2
Equivalent Diameter (φ)

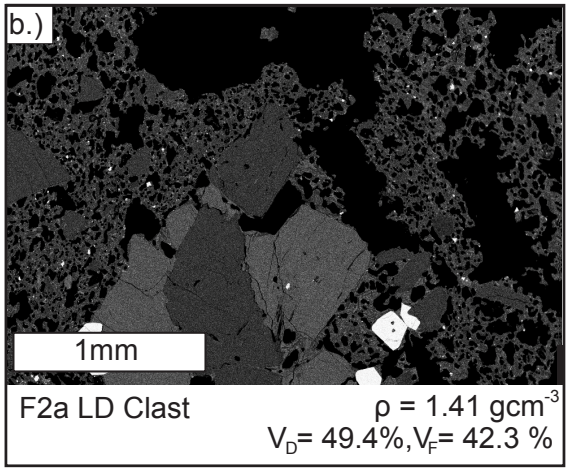
b.)
1mm
F2a LD Clast
ρ = 1.41 gcm-3
VD= 49.4%,VF= 42.3 %

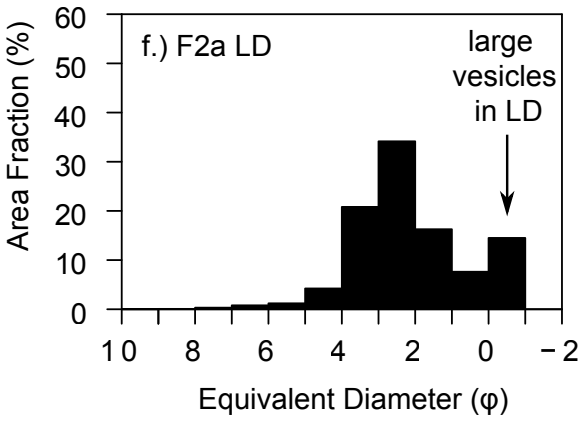
f.) F2a LD
large vesicles in LD
Area Fraction (%)
60
50
40
30
20
10
0
10 8 6 4 2 0 −2
Equivalent Diameter (φ)

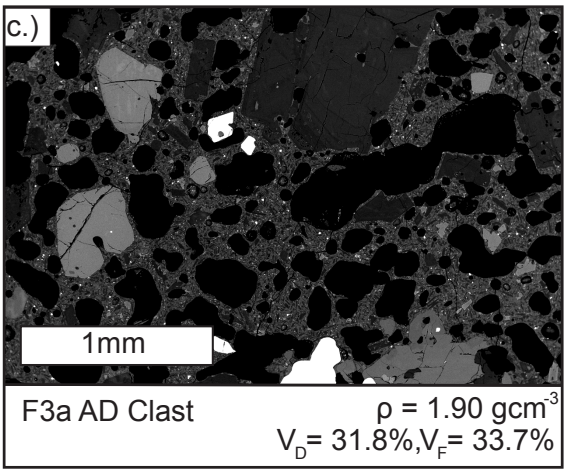
c.)
1mm
F3a AD Clast
ρ = 1.90 gcm-3
VD= 31.8%,VF= 33.7%

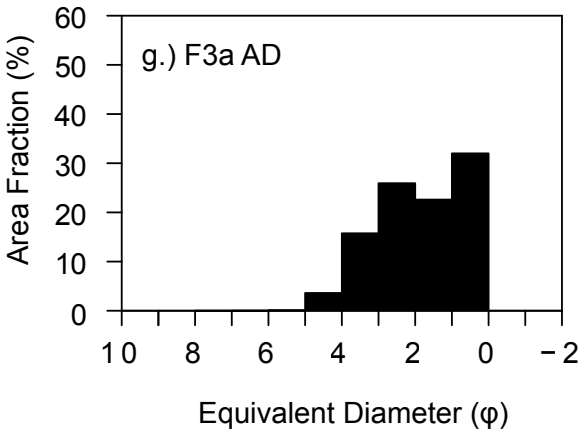
g.) F3a AD
Area Fraction (%)
60
50
40
30
20
10
0
10 8 6 4 2 0 −2
Equivalent Diameter (φ)

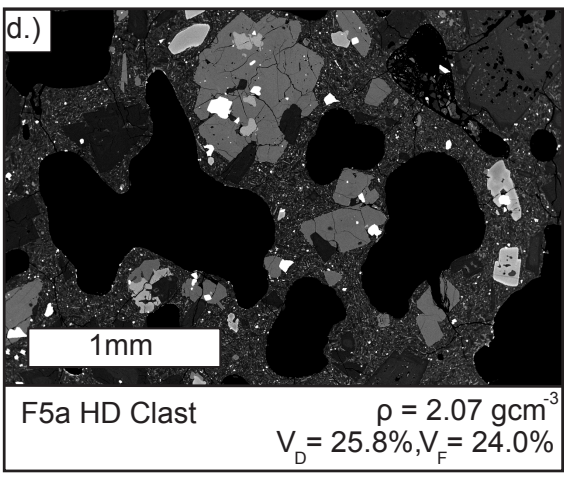
d.)
1mm
F5a HD Clast
ρ = 2.07 gcm-3
VD= 25.8%,VF= 24.0%

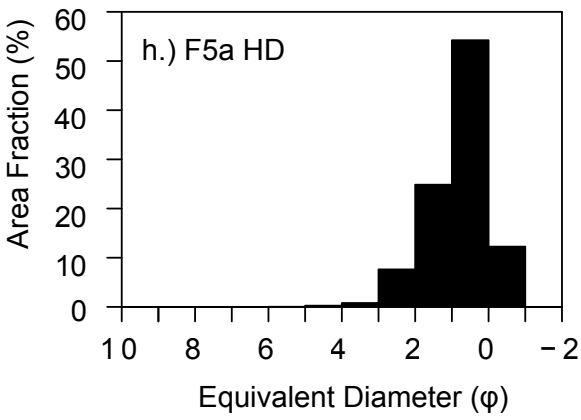
h.) F5a HD
Area Fraction (%)
60
50
40
30
20
10
0
10 8 6 4 2 0 −2
Equivalent Diameter (φ)

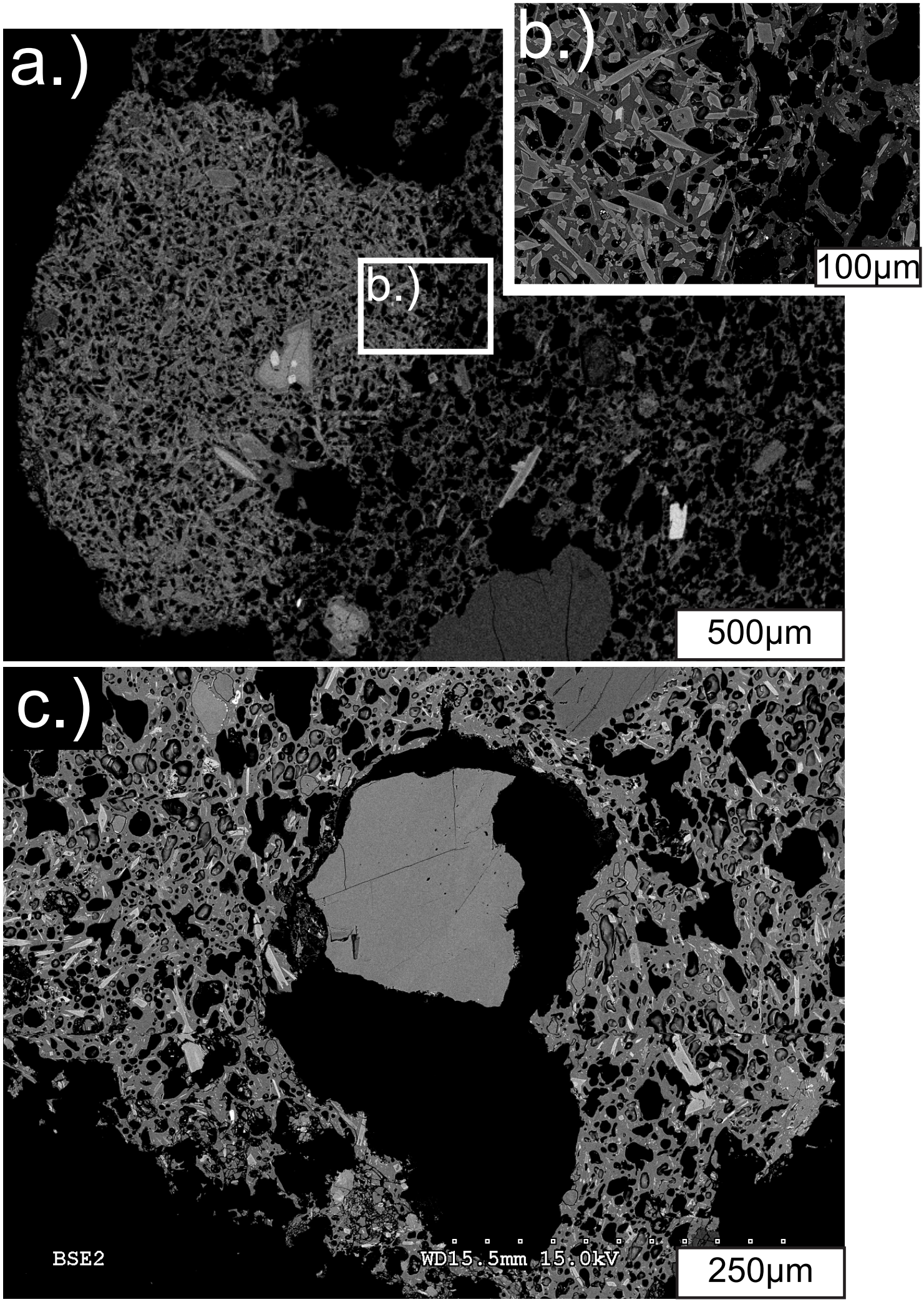
a.)
b.)
100µm
b.)
500µm
c.)
BSE2
WD15.5mm 15.0kV
250µm

FUEGO

AVELLINO

a.) Expected trend (F3a)

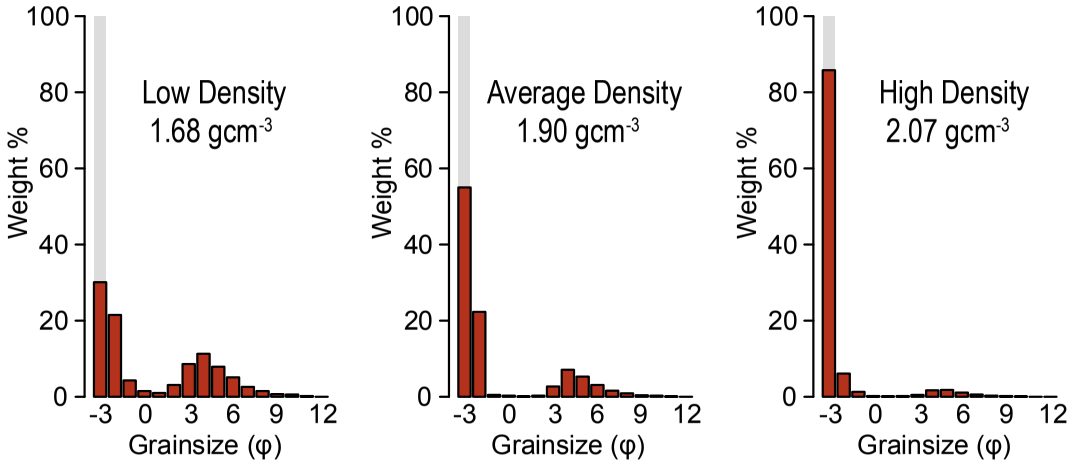

b.) Expected trend (Av33a)

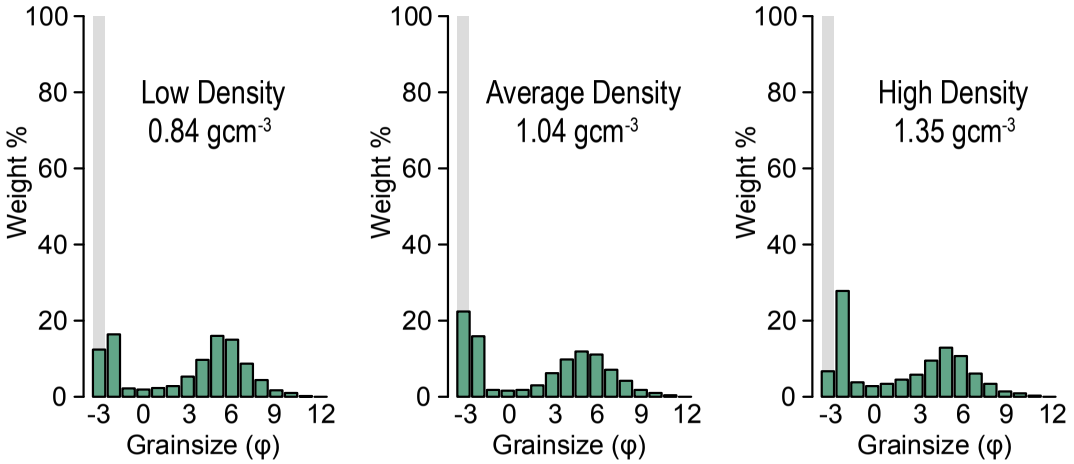

c.) Unexpected trend (F2a)

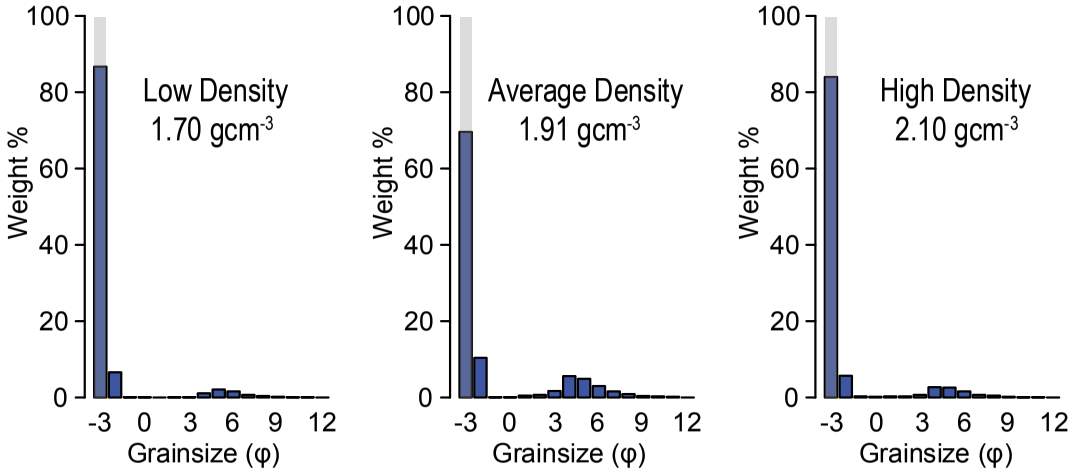

d.) Unexpected trend (Av31a)

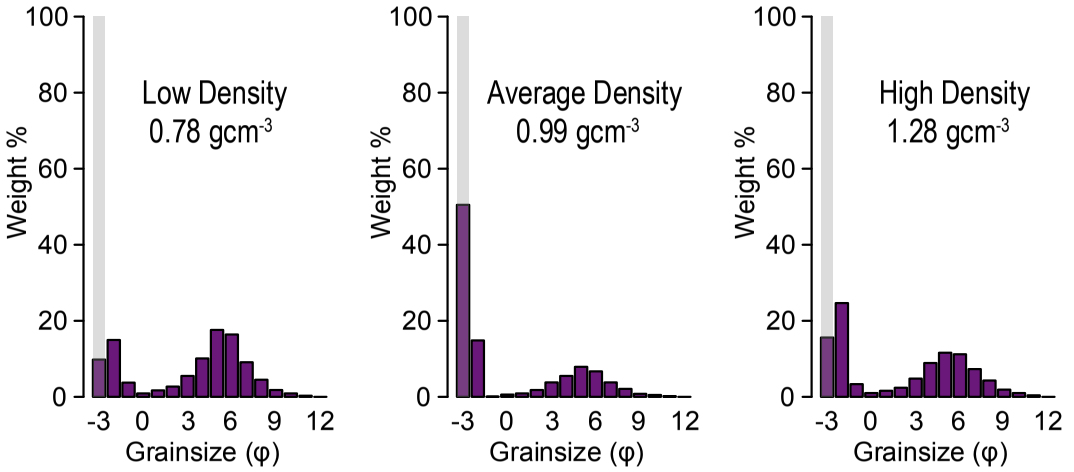

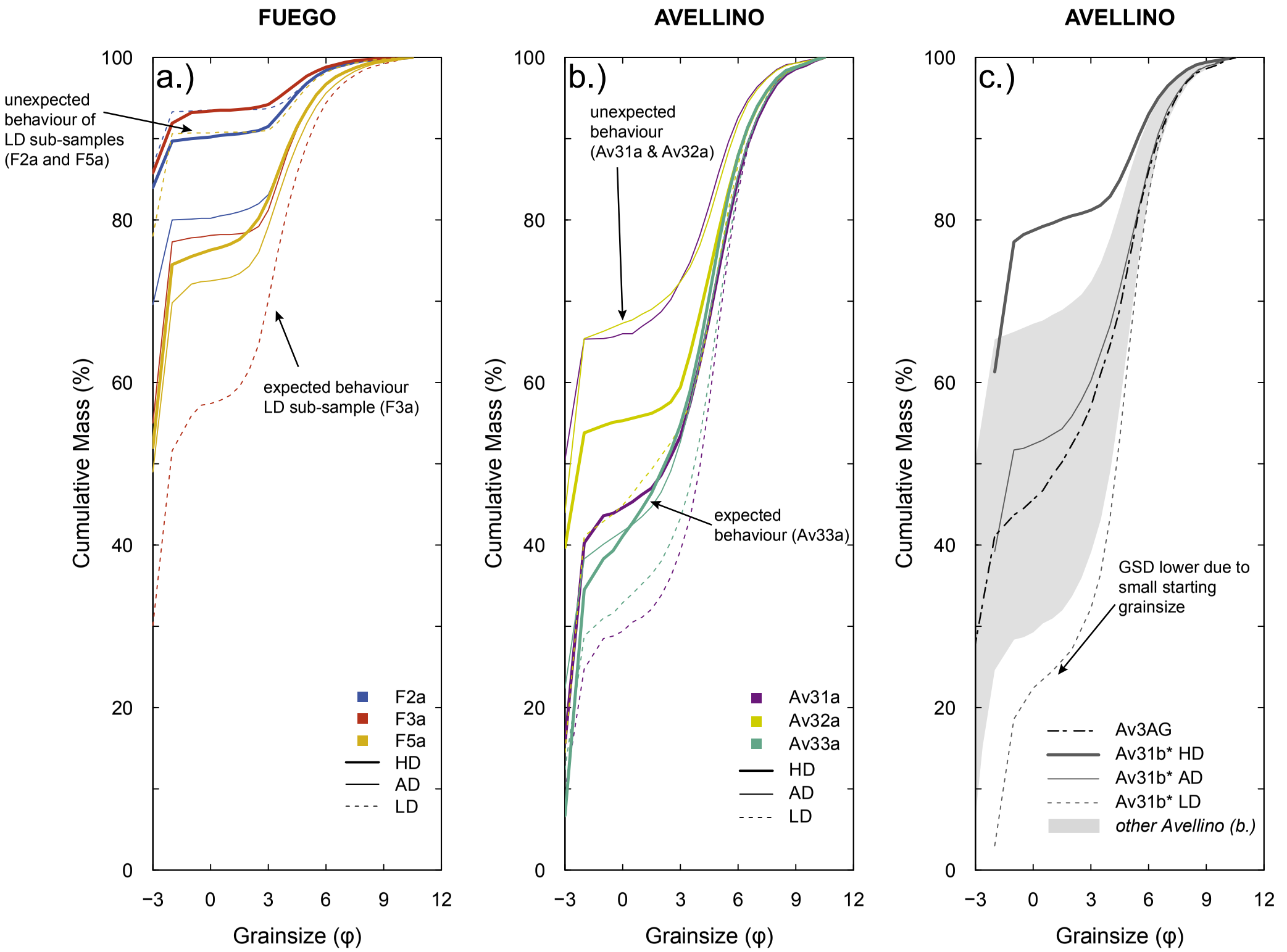
FUEGO
AVELLINO
AVELLINO
a.)
b.)
c.)
unexpected behaviour of LD sub-samples (F2a and F5a)
expected behaviour LD sub-sample (F3a)
unexpected behaviour (Av31a & Av32a)
expected behaviour (Av33a)
GSD lower due to small starting grainsize
Cumulative Mass (%)
Grainsize (φ)
F2a
F3a
F5a
HD
AD
LD
Av31a
Av32a
Av33a
Av3AG
Av31b* HD
Av31b* AD
Av31b* LD
other Avellino (b.)

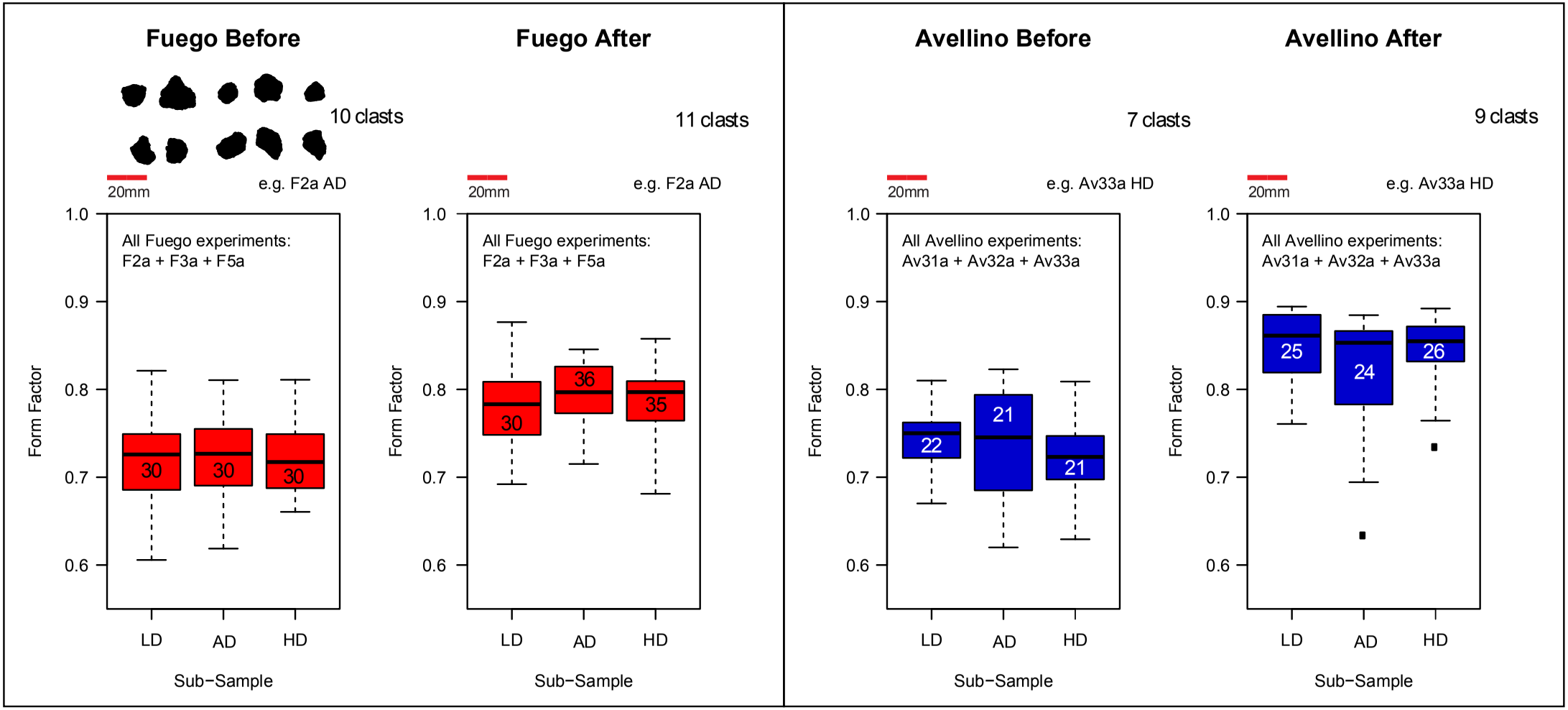
Fuego Before
10 clasts
20mm
e.g. F2a AD
All Fuego experiments:
F2a + F3a + F5a
Form Factor
1.0
0.9
0.8
0.7
0.6
30
30
30
LD
AD
HD
Sub−Sample
Fuego After
11 clasts
20mm
e.g. F2a AD
All Fuego experiments:
F2a + F3a + F5a
Form Factor
1.0
0.9
0.8
0.7
0.6
30
36
35
LD
AD
HD
Sub−Sample
Avellino Before
7 clasts
20mm
e.g. Av33a HD
All Avellino experiments:
Av31a + Av32a + Av33a
Form Factor
1.0
0.9
0.8
0.7
0.6
22
21
21
LD
AD
HD
Sub−Sample
Avellino After
9 clasts
20mm
e.g. Av33a HD
All Avellino experiments:
Av31a + Av32a + Av33a
Form Factor
1.0
0.9
0.8
0.7
0.6
25
24
26
LD
AD
HD
Sub−Sample

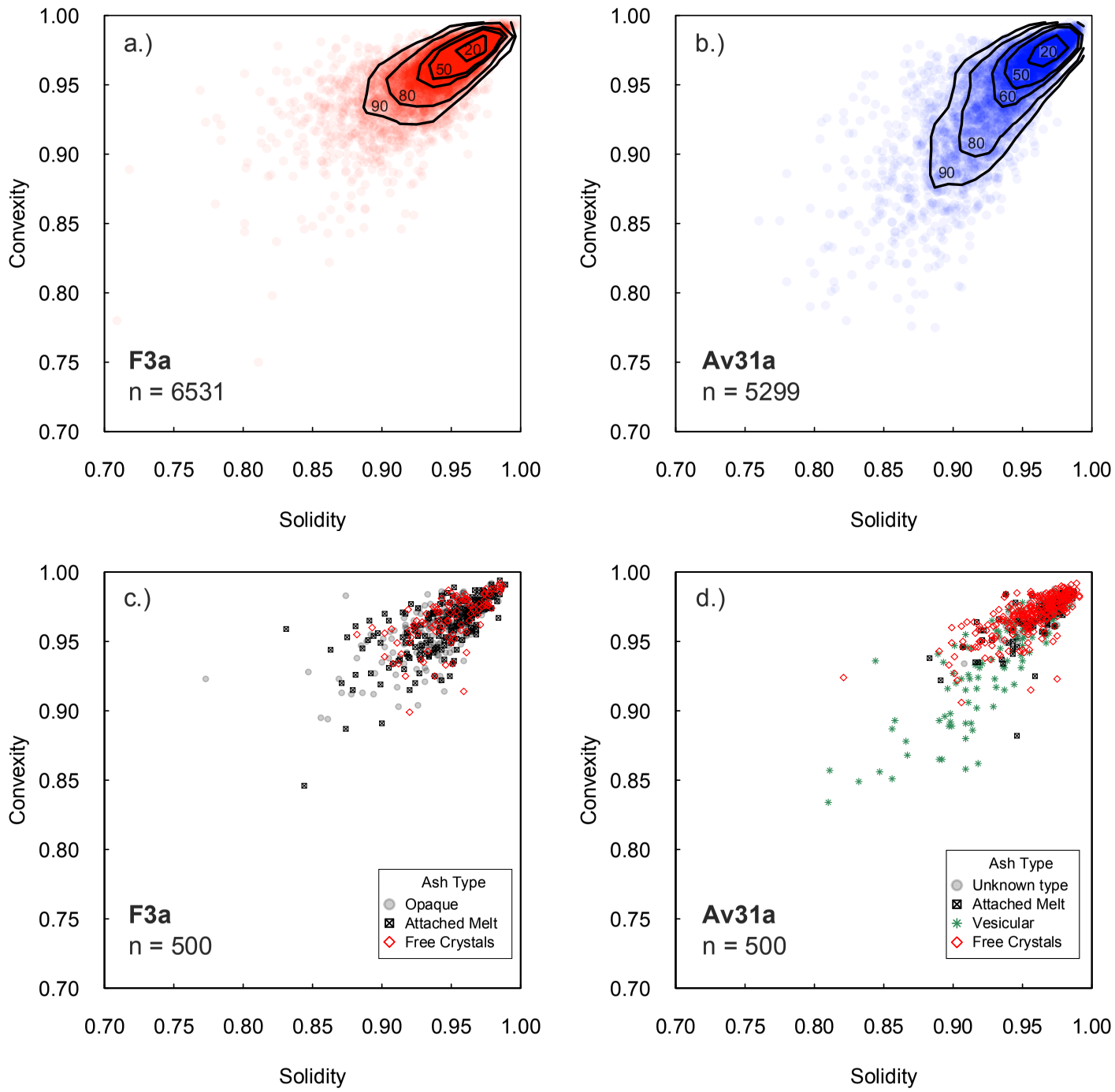
a.)
F3a
n = 6531
20
50
80
90
b.)
Av31a
n = 5299
20
50
60
80
90
c.)
F3a
n = 500
Ash Type
Opaque
Attached Melt
Free Crystals
d.)
Av31a
n = 500
Ash Type
Unknown type
Attached Melt
Vesicular
Free Crystals
Convexity
Solidity
1.00
0.95
0.90
0.85
0.80
0.75
0.70

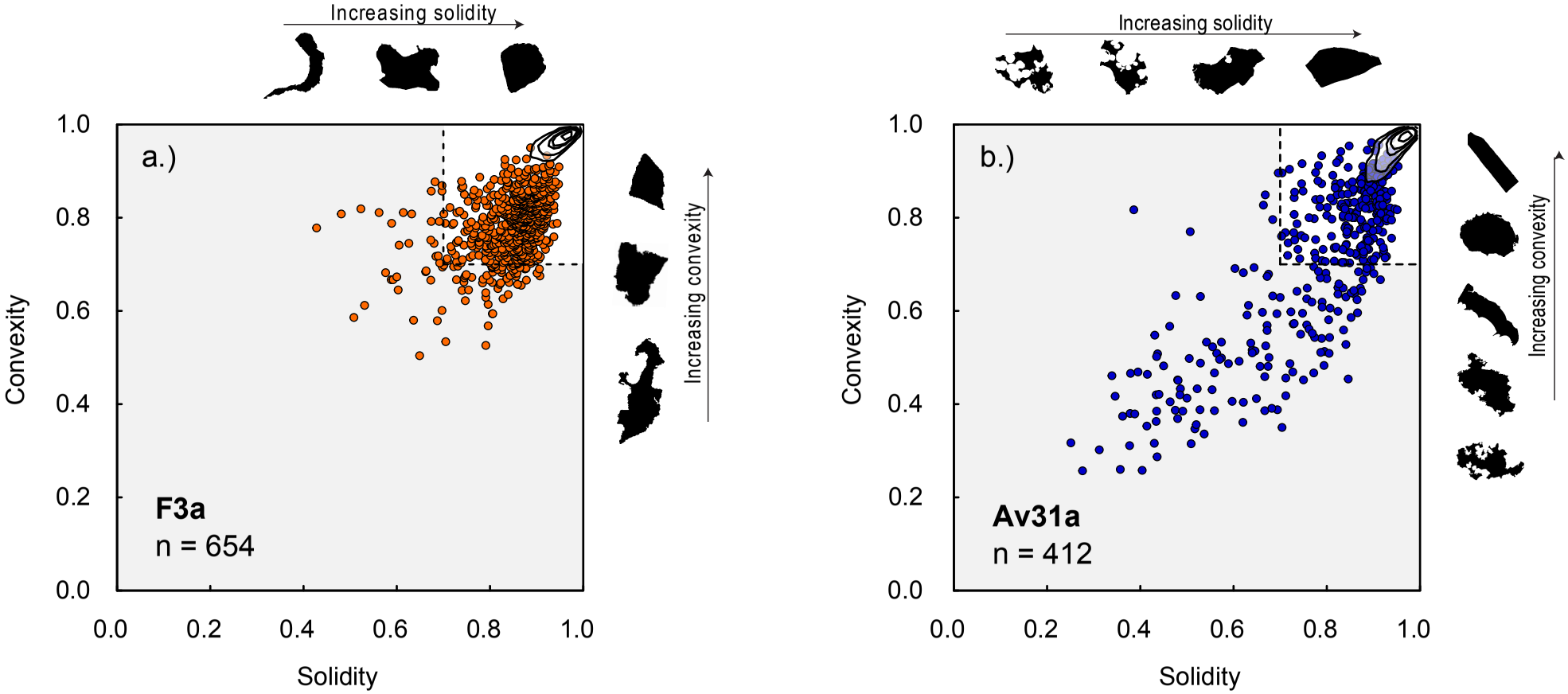
Increasing solidity
a.)
F3a
n = 654
Convexity
Solidity
Increasing convexity
1.0
0.8
0.6
0.4
0.2
0.0
0.0
0.2
0.4
0.6
0.8
1.0
Increasing solidity
b.)
Av31a
n = 412
Convexity
Solidity
Increasing convexity

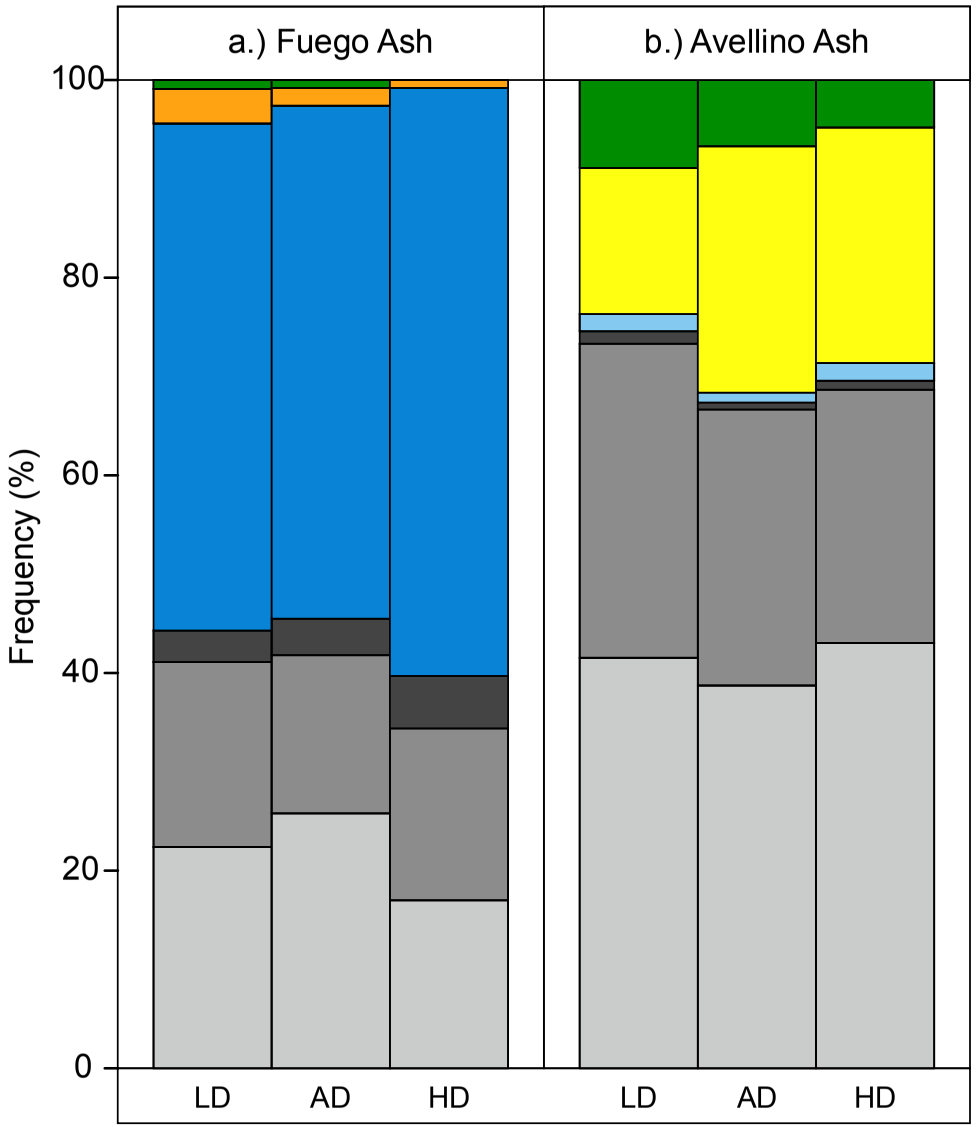

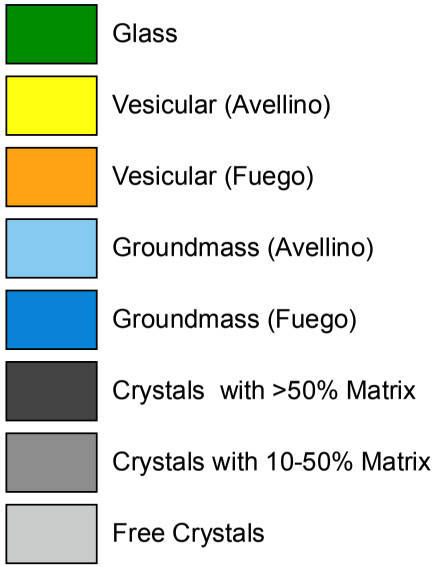

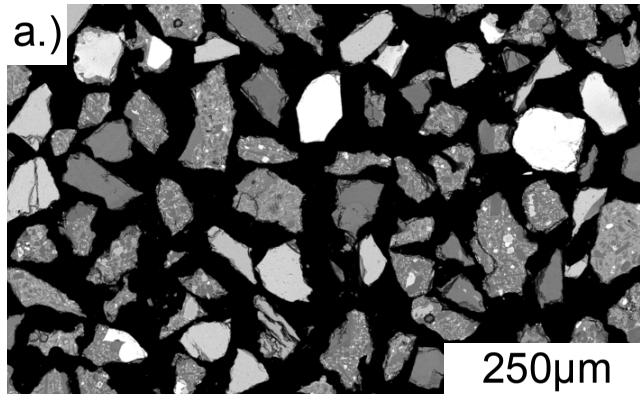

F3a AD 3φ

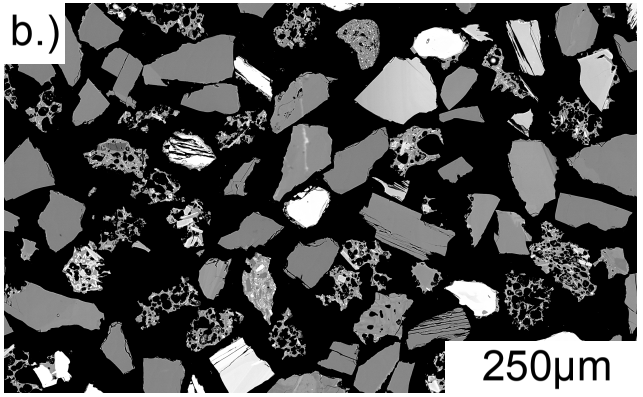

Av31a AD 3φ

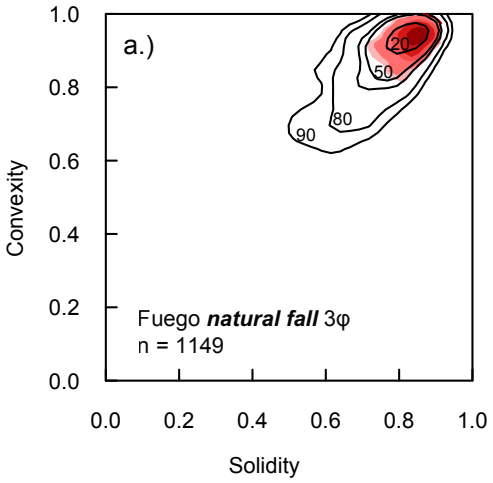

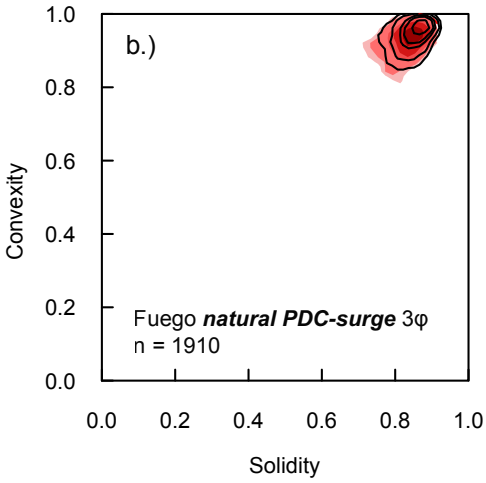

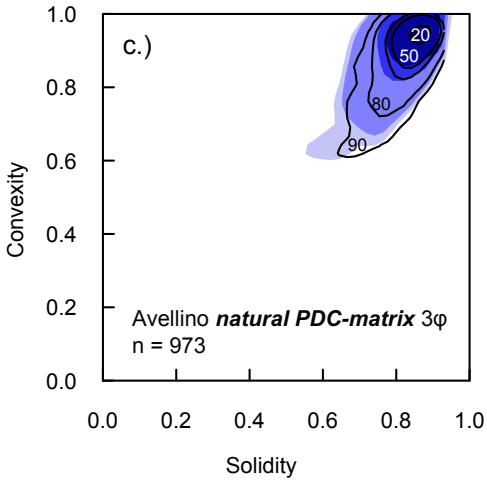

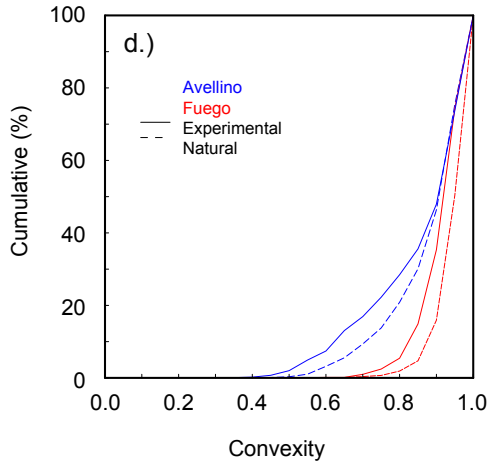

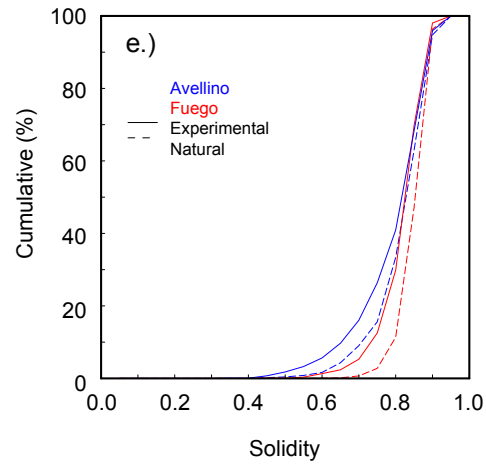

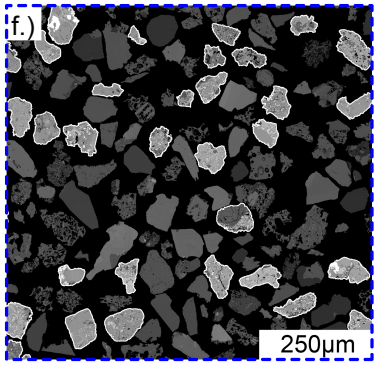

Natural PDC-matrix Avellino 3φ
large lithic component

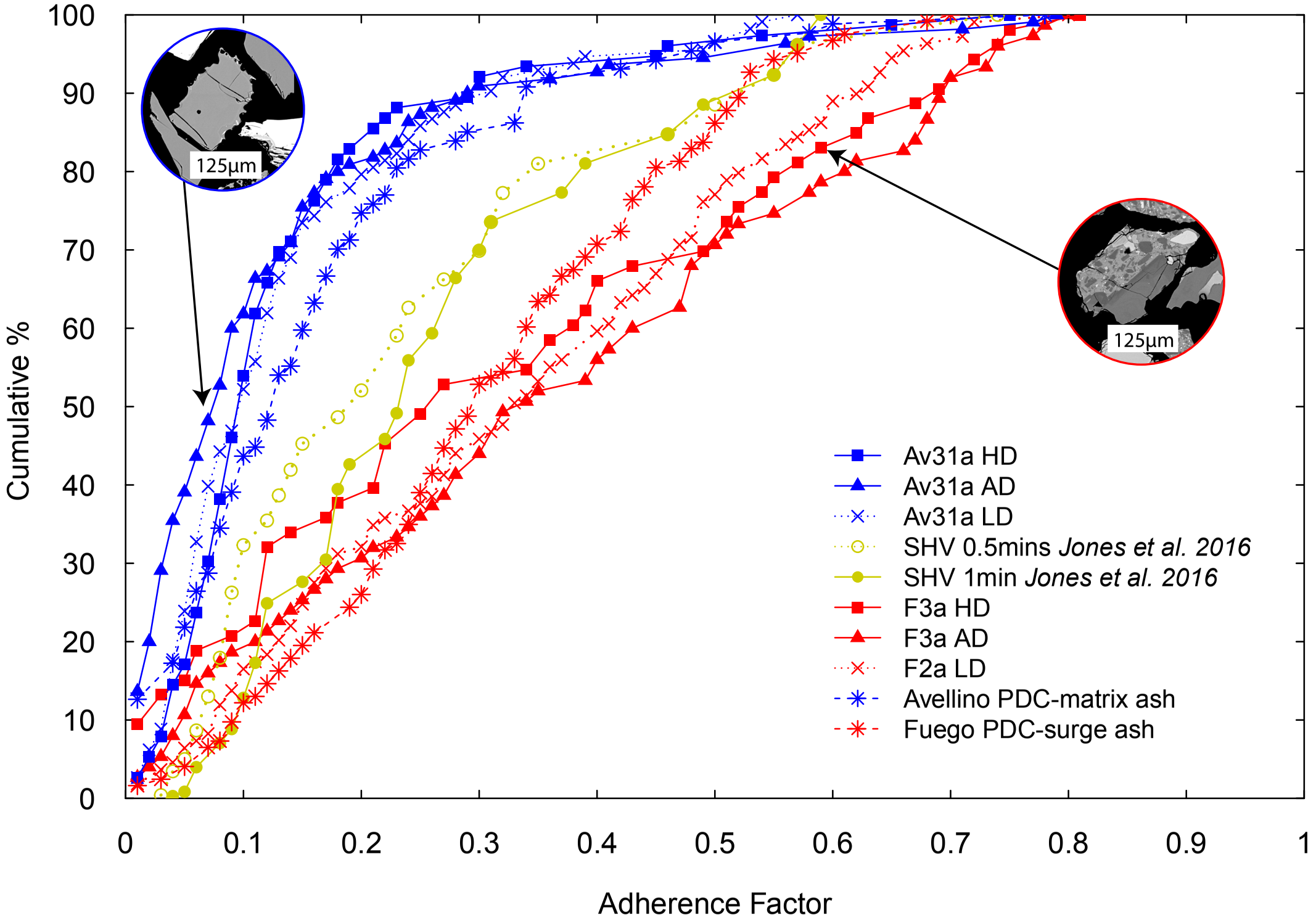
Cumulative %
Adherence Factor
0
10
20
30
40
50
60
70
80
90
100
0
0.1
0.2
0.3
0.4
0.5
0.6
0.7
0.8
0.9
1
125µm
125µm
Av31a HD
Av31a AD
Av31a LD
SHV 0.5mins Jones et al. 2016
SHV 1min Jones et al. 2016
F3a HD
F3a AD
F2a LD
Avellino PDC-matrix ash
Fuego PDC-surge ash